Icarus 434 (2025) 116538

Contents lists available at ScienceDirect

Icarus

journal homepage: www.elsevier.com/locate/icarus

Research Paper

The mineralogical composition of Jezero Crater Western Fan: Multigaussian modeling of *Perseverance*/SuperCam near-infrared observations and overview of major units

C. Royer [a,b,*], F. Poulet [c], R.C. Wiens [b], F. Montmessin [a], P. Beck [d], O. Beyssac [e], É. Clavé [f], E. Dehouck [g], T. Fouchet [h], J.R. Johnson [i], L. Mandon [d], S. Bernard [e], G. Caravaca [j], S. le Mouélic [k], C. Pilorget [c,l], C. Quantin-Nataf [g], S. Maurice [j], A. Cousin [j]

[a] *LATMOS/IPSL, UVSQ Université Paris-Saclay, Sorbonne Université, CNRS, Guyancourt, France*
[b] *Purdue University Earth, Atmospheric and Planetary Sciences department, West Lafayette, IN, USA*
[c] *Institut d'Astrophysique Spatiale, CNRS/Paris-Saclay University, France*
[d] *Université Grenoble-Alpes, CNRS, IPAG, UMR 5274, Grenoble, France*
[e] *Institut de Minéralogie, de Physique des Matériaux et de Cosmochimie, CNRS, Sorbonne Université, Muséum National d'Histoire Naturelle, Paris, France*
[f] *Deutsches Zentrum für Luft- und Raumfahrt e.V. (DLR), Institut für Optische Sensorsysteme, 12489 Berlin, Germany*
[g] *Université de Lyon, UCBL, ENSL, CNRS, LGL-TPE, Lyon, France*
[h] *LESIA, Observatoire de Paris, Université PSL, CNRS, Sorbonne Université, Université de Paris, Meudon, France*
[i] *Johns Hopkins University Applied Physics Laboratory, Laurel, MD, USA*
[j] *IRAP, CNRS, Université de Toulouse, UPS-OMP, Toulouse, France*
[k] *Nantes Université, Univ Angers, CNRS, UMR 6112, Laboratoire de Planétologie et Géosciences, F-44000 Nantes, France*
[l] *IUF, Institut Universitaire de France, Paris, France*

ARTICLE INFO

Keywords:
Mars
Infrared spectroscopy
Planetary mineralogy

ABSTRACT

The analysis of the mineralogical composition of rocks within the Jezero crater, Mars, enables the reconstruction of the aqueous activity history of the site, formed during the planet's early epochs. Numerous secondary minerals resulting from aqueous alteration, as well as some primary minerals, are observable through near-infrared reflectance spectroscopy, as performed by the IRS/SuperCam instrument onboard the *Perseverance* rover. The characterization of these minerals, their distribution within geological units, as well as the composition of their assemblages, is crucial for deciphering the chemical, climatic, and geological history of the Jezero crater. In order to systematically study the growing number of IR spectra collected by the instrument, we have developed an automated method for extracting the characteristics of absorption bands, based on their modeling using a combination of Gaussian curves (MultiGM). The application of this method to the entire IRS dataset reveals a significant diversity of minerals distributed throughout the rover traverse, with a near-systematic presence of phyllosilicates in bedrocks, as well as increasingly frequent occurrences of carbonates on the delta, particularly within the Margin unit. These carbonates exhibit variable 2.5 μm band positions attributed to different Fe and Mg compositions. The delta front presents the sole unit generally enriched in Fe/Mg sulfates (Yori Pass/Hogwallow Flats) accompanied by occurrences of bassanite (hydrated $CaSO_4$), whereas the presence of sulfates in other delta units and the crater floor is more sporadic and corresponds to fracture/vesicle fills. Finally, almost all the rocks analyzed with IRS/SuperCam are notably dominated by phyllosilicates signatures (Fe/Mg-smectites, serpentine), excepted for a few outcrops caping the Delta. This phyllosilicate presence witnesses the extended surficial (smectites) and hydrothermal (serpentine) aqueous alteration of Jezero's rocks, either *in situ* or carried from the watershed.

* Corresponding author at: LATMOS/IPSL, UVSQ Université Paris-Saclay, Sorbonne Université, CNRS, Guyancourt, France.
E-mail address: clement.royer@latmos.ipsl.fr (C. Royer).

https://doi.org/10.1016/j.icarus.2025.116538
Received 25 May 2024; Received in revised form 14 February 2025; Accepted 25 February 2025
Available online 7 March 2025

1. Introduction

1.1. The perseverance rover in Jezero crater

The *Perseverance* rover landed in Jezero Crater on February 18, 2021 (Farley et al., 2020). A major geological feature of this crater is its western sedimentary fan, inferred to have formed in a deltaic environment during the Hesperian era, the crater itself being formed during the Noachian (Fassett and Head, III, 2005; Mangold et al., 2020). This landform, hereafter referred to as a delta is one of several indicators suggesting that Jezero may have hosted a closed-lake environment estimated to have lasted between 10^6 and 10^7 years (Schon et al., 2012). Mineralogical observations from orbital missions, specifically using the Compact Reconnaissance Imaging Spectrometer for Mars (CRISM) onboard the NASA Mars Reconnaissance Orbiter (MRO) (Murchie et al., 2007), have identified numerous alteration phases related to fluid-rock interaction (carbonates, phyllosilicates, hydrated silica) within Jezero's delta and surrounding terrains (Goudge et al., 2015a; Tarnas et al., 2019; Horgan et al., 2020; Carter et al., 2023). Since landing, the *Perseverance* rover has explored various geological units of the crater floor and delta, revealing a significant diversity in rock textures, outcrops, and both geochemical and mineralogical compositions (Farley et al., 2022). The Crater floor is divided into two primary geological units: Máaz and Séítah, both of igneous origin but with markedly different compositions. Based on remote sensing observations and contact measurements of selected targets, Máaz shows a basaltic composition with pyroxenes and feldspars, as well as sulfates and other limited secondary minerals (Fe^{3+}-phyllosilicates and oxyhydroxides) (Wiens et al., 2022; Mandon et al., 2023; Udry et al., 2023; Corpolongo et al., 2023). Séítah is composed of olivine-rich cumulates with evidence of limited aqueous alteration in the form of phyllosilicates, carbonates, and sulfates, this latter identified in fracture/vesicle fill (Wiens et al., 2022; Liu et al., 2022; Tice et al., 2022; Mandon et al., 2023; Beyssac et al., 2023; Clavé et al., 2023; Corpolongo et al., 2023).

In the delta overlying the Crater floor, two regional units are distinguishable: the delta front (Shenandoah formation, Stack et al. 2024), and the upper delta (Tenby formation, Ives et al. 2023, Siebach et al. 2024) (Fig. 1). The delta front is characterized by sedimentary strata, up to 25 meters thick, ranging from fine to coarse grain sandstone and pebble conglomerate (Mangold et al., 2021; Stack et al., 2024). This region exhibits significant mineralogical diversity, prominently featuring sulfates, and phyllosilicates (Dehouck et al., 2023; Jones et al., 2023; Hurowitz et al., 2023). The Margin unit, at the mouth of Neretva Vallis, as well as the Tenby formation, show an increasing carbonate presence within variably altered rocks, locally accompanied by sulfates (Clavé et al., 2024; Siebach et al., 2024). Additionally, a series of minimally altered boulders, rich in olivine and pyroxene, have been identified, likely remnants of either a capping unit or a late-stage fluvial deposit at the stratigraphic top (Beyssac et al., 2024; Dehouck et al., 2024; Moreland et al., 2024; Gwizd et al., 2024). The alteration minerals noted above are of significant interest for Martian exploration because of their formation by interaction with liquid water, possibly under distinct geochemical conditions. However, to constrain the precise conditions of their formation, it is necessary to finely characterize their assemblages in relation to the geochemical and textural context. We aim to investigate this aspect comprehensively across the entire traverse of the rover, from the Crater floor to the Margin unit. This overarching perspective on the data facilitates contextualizing mineral detections by assessing their frequency of occurrence and their relationship with the local bedrock geology and among the geological units. Given the large volume of spectra acquired from landing to the present study (~ 1100 Sols, ~ 900 SuperCam observations generating ~ 6700 near-infrared (NIR) spectra), we propose an automated approach to analyze NIR spectra acquired in the 1.3–2.6 μm range with the SuperCam instrument's Infrared Spectrometer (IRS) (Maurice and Wiens, 2021; Wiens et al., 2021; Fouchet et al., 2022).

1.2. Needs and challenges of near-infrared spectral modeling

The objective of spectral analysis in the NIR is to infer the properties of the observed material from studying the reflectance spectrum's characteristics, such as the presence of absorption bands, their position, depth, width, multiplicity, shape (*e.g.*, convexity), the presence of overall slope or curvature in the spectrum, etc. These properties depend on a multitude of physical parameters (nature of absorbers, grain size, matrix effects, porosity, coatings) and observational factors (incidence angle, phase angle, atmospheric scattering by dust), in a nonlinear and highly degenerated manner: multiple sets of parameters can sometimes lead to the same reflectance spectrum. The challenge of spectral modeling, therefore, is to propose a model that physically describes the light-matter interaction to constrain the mineralogy and physical properties of the observed rock. However, due to the complexity of real rocks, commonly used radiative transfer models (*e.g.*, proposed by Shkuratov et al. 1999 and Hapke 1981, 1993) rely on simplifying hypotheses that are not easily applicable to all observations (*e.g.*, granular medium) or require knowledge of parameters that are not well documented in the literature (*e.g.*, optical constants of all candidate minerals), and knowledge of local surface facet orientations that are not readily available without detailed topographic modeling or inaccessible during observation (*e.g.*, local phase angle).

A simpler approach is to model NIR spectra using a linear combination of reflectance spectra, including methods such as SMA (Spectral Mixing Analysis Adams et al. 1986, Merényi et al. 1996), and MELSUM (Multiple-Endmember Linear Spectral Unmixing Model Combe et al. 2008, Le Mouelic et al. 2009, Johnson et al. 2007). We acknowledge that such linear methods are an incomplete representation of complex (intimate) physical mixtures, and that the calculation of mixing coefficients is intended to detect the presence, but not the actual abundances, of candidate minerals.

In the approach used here, we do not seek to deduce the intrinsic physical properties of the rock but rather to reduce the dimensionality of the spectral parameter space by using a Multi-Gaussian Modeling (MultiGM) analysis of absorption bands. This method is similar to the Modified Gaussian Model (MGM) (Sunshine et al., 1990) as it involves fitting a linear combination of Gaussian curves to the data, but it differs in that the Gaussian curves are not individually studied. Instead, multiple Gaussian curves serve as a way to interpolate an entire spectrum. MultiGM method is not intended to be more performant than other band fitting methods (*e.g.*, Brown 2006, Parente et al. 2011) or algorithms specifically designed for spectral identification (*e.g.*, Tetracorder, Clark et al. 2003, Dalton 2003). For instance, Brown (2006) demonstrated that when modeling absorption bands in the SWIR, using Lorentzian, Gaussian, or pseudo-Voigt profiles does not drastically affect the fit quality. In fact, Gaussian profiles often perform better when applied to spectra with a continuum already removed, which is the case in our work. Similarly, Parente et al. (2011) evaluated the precision of absorption band analysis using various methods, including Gaussian modeling, the MGM (Modified Gaussian Model), and the Levenberg–Marquardt algorithms, while discussing the relevance of continuum removal or modeling techniques. They concluded that the LM algorithm produces results similar to MGM and that, depending on the minerals or their mixtures, MGM and unmodified Gaussians can yield comparable results. Furthermore, Sunshine et al. (1990), who described the MGM, also noted that modifying Gaussian profiles allows for the asymmetry of absorption bands to be captured and provides a potential physical interpretation for each Gaussian endmember describing the bands. In our case, we chose to subtract the continuum rather than model it, using a convex upper hull as described in Parente et al. (2011). This approach is well-suited for Gaussian modeling, as outlined in Brown (2006). Additionally, we opted for unmodified Gaussians to prioritize simplicity over the physical representativeness of the endmembers. Ultimately, this choice achieves a similar outcome: fitting the bands to calculate their position, width, depth, and area.

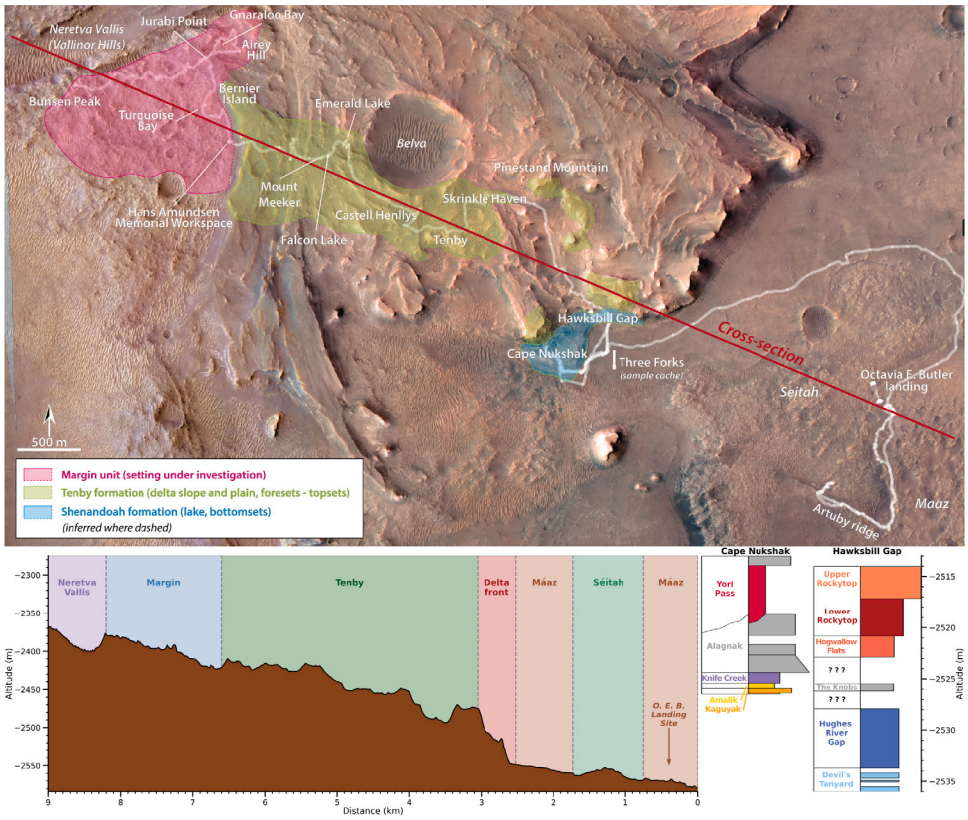

Fig. 1. (Top) Overview of Jezero crater western fan's main regional units. The white line is the rover pathway. Valinor Hills is the ultimate location of Ingenuity. (Bottom left) Variation of the surface altitude along the cross section (red line in the upper panel) with the delimitation of the main regional features. (Bottom right) Simplified stratigraphic column of the two lobes explored by the rover in the Delta front: Cape Nukshak on the West, Hawksbill Gap on the East. Strata coloring follows the same color code as in Figs. 7 to 10. (For interpretation of the references to color in this figure legend, the reader is referred to the web version of this article.)
Source: Adapted from Stack et al. (2024).

Other methods for reducing the dimensionality of the dataset, such as Principal Component Analysis (PCA) or Independent Component Analysis (ICA), can also help separate the dominant mineral components in the form of eigenvectors. However, these eigenvectors and their associated eigenvalues only have statistical significance, and apart from the position of the absorption bands, they are difficult to interpret. Studies have been initiated using these techniques on IRS/SuperCam data (Mandon et al., 2023), but their interpretation has been complex and ultimately inconclusive compared to the direct study of absorption bands.

1.3. General approach

The objective is to group IRS observations into a parameter space suitable for classifying spectra with subtle differences. NIR spectra exhibit absorption features that reflect chemical bonds in specific environments (molecular or crystalline), providing diagnostic information about minerals (see Section 2.1). However, many absorption bands resemble those of multiple minerals, among different mineral families (*e.g.*, the 2.3 μm band present in both carbonates and phyllosilicates), and they are influenced by several factors, complicating confident mineral attribution for spectral features. Comparing band centers and relative band areas aids in identifying the minerals responsible for observed spectral features, as acknowledged in previous studies. The approach employed in this paper is based on multi-Gaussian modeling, extensively used for Mars and other planetary bodies (see Section 2.1). The visible range (0.5–0.85 μm) of SuperCam is not considered in this study because of its smaller field of view (0.74 mrad vs. 1.15 mrad for the IRS), which is not as representative of a bulk rock observation, and the different fidelity of their absolute calibration. The data we use have been calibrated into reflectance using the rover's onboard white calibration target (Manrique et al., 2020) and an instrumental model described by Royer et al. (2023). Data were filtered to exclude target locations acquired in shadow and those that were out of focus or blocked by hardware. All data are accessible through the NASA Planetary Data System (Maurice et al., 2021).

1.4. Paper outline

This paper is structured as follows. Section 2 provides a detailed presentation of the MultiGM method that we developed, including its overarching objectives (2.1), algorithmic specifics (2.2), application to laboratory spectrum separation (2.3), and discussion of its advantages and limitations (2.4). Following this, Section 3 presents all results obtained from applying the MultiGM method to SuperCam observations up to Sol ~ 1100 (see Section 3.1 for a description of how we selected the dataset), covering the four main regional areas visited by the rover: the Crater floor (3.2), the Shenandoah formation (3.3), the Tenby formation (3.4), and the Marginal unit (3.5). Finally, the discussion (Section 4) summarizes our findings (4.1) by comparing them across units and between different instruments of *Perseverance* (4.2).

2. Assessing the complexity of mineral assemblages: the multi-Gaussian modeling

2.1. Objectives

A first approach to analyzing reflectance spectra is to identify the absorption bands and determine their position in order to deduce the nature of the absorbents. In the NIR, between 1.3 and 2.6 μm in

the case of IRS, absorption bands originate from various sources as vibrational transitions of one or more chemical bonds between atoms, transition states of Fe^{2+} in olivine and pyroxene, or crystalline lattice modes (Hunt and Salisbury, 1970; Burns, 1970, 1993; Califano et al., 1981; Clark et al., 1990; Carter et al., 2013).

Some absorption features in the near-IR are known to be diagnostically linked to specific mineral families (*e.g.*, the 1.4 μm triplet of gypsum, $CaSO_4{\cdot}2H_2O$) or their combination with another band is also diagnostic of the mineral family (*e.g.*, the 2.3 and 2.5 μm bands in carbonates). Other absorption features are less diagnostic because they are present in many different species, such as the water-related absorptions at 1.4 and 1.9 μm, but their precise position and shape in association with other absorption bands may be used to discriminate between minerals, or at least mineral families (Bishop et al., 2008). Another variable of interest is the depth of the bands, which is linked to the amount of absorbent but also to grain size. The relative depths of absorption bands are also a good indicator of the presence of a mineral species (*e.g.*, 2.5 μm/2.3 μm band depth ratio in calcite is typically 1.5–2.0 Bishop et al. 2021).

Analyses become more complicated when several species with similar absorption bands contribute to the observed absorption spectrum. Their spectral characteristics then mix, distorting the absorption bands, shifting slightly their position or forming combinations of bands that are more difficult to interpret. For example, the presence of sulfates or Fe-hydroxides (ferrihydrite, goethite) in a mixture of Fe/Mg-phyllosilicates can result in a broadening of the hydration band at 1.9 μm and a distortion of the Fe-OH band at 2.3 μm.

The multi-Gaussian modeling (MultiGM) of absorption bands has been considered as an efficient way to model the shape and the depth of the spectral signatures in the near-infrared wavelength (*e.g.*, Kanner et al. 2007 and references therein). A similar approach has been already applied to various VISIR orbital datasets to interpret the composition of mafic-bearing terrains of the Moon (*e.g.*, Isaacson et al. 2011), Mars (*e.g.*, Clenet et al. 2013) or laboratory data (Pinet et al., 2022). The MultiGM approach is here adapted to reproduce both strong and broad bands associated with primary minerals (*e.g.*, olivine, pyroxene) as well as weak and narrow bands, which track the alteration products that are present in the rocks analyzed by IRS/SuperCam. This method provides an analytical expression for each absorption band, so that its position can be extracted with great precision (< 5 nm average) for checking consistency between the position of different species (*e.g.*, 1.4 μm vs metal-OH positions, Ehlmann et al. 2009). It also enables band areas to be calculated and compared with each other. The advantage of the band area compared to the band depth is directly related to the amount of energy locally absorbed, such that its distribution among the absorption bands of a species can be diagnostic of this species.

The surfaces of the extracted absorption bands are then projected onto selected ternary diagrams in order to distinguish the dominant mineral components of the mixture, and the distributions of the positions of the studied bands are analyzed to more precisely identify the minerals present.

2.2. Method and derived observables

The entire method detailed in this section has been developed for the study of IRS spectra. It is based on the automatic detection of absorption bands in predefined spectral ranges (Table 1).

Before the retrieval of the parameters of interest (band minimum position, band depth and band area), the analysis is performed according to several steps described hereafter.

- Data smoothing using a Savitzky-Golay filter (Savitzky and Golay, 1964; Steinier et al., 1972) of degree 3 and with a window of 9 spectral channels. This smoothing step is not systematically performed; it is only used on noisy data (SNR < 60) to make the detection of the band shoulders more accurate. This filter and its parameters have been selected to preserve the absorption features shape.

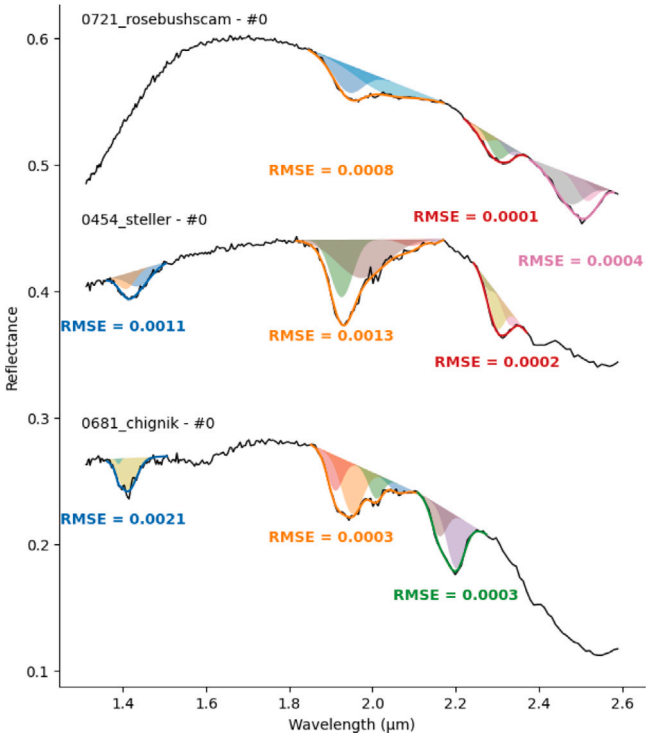

Fig. 2. Examples of MGM fit of absorption bands in SuperCam/IRS observations. The naming convention here is Sol number_target name_raster position starting, at 0. Several Gaussian are required to fit each major signature within 1.4, 1.9, 2.2–2.5 μm ranges. The quality of the fit is estimated using root mean square error (RMSE).

- First band minimum position estimate: in the defined spectral range (see Table 1), the local minimum is simply detected.
- Band shoulders detection: in the defined spectral range the continuum is estimated as a straight line tangentially joining the shoulders of the band. This tangent line is determined using a convex upper hull algorithm (Scipy ConvexHull and Clark and King 1987) fitting the spectrum with a collection of tangent segments. The segment representing the continuum is therefore the one above the band minimum.
- Continuum removal: division of the spectrum between the detected shoulders by the local continuum, defined as a straight line.
- Multi-Gaussian fit: using a least squares minimization algorithm, the continuum-removed spectrum is fitted by a sum of up to 4 Gaussian curves representing the data with up to 12 parameters (position, width and amplitude of each Gaussian, Fig. 2).
- Retrieval of the band minimum position, band depth and band area.

A good way to visualize the variation of the energy distribution of the spectral signatures of interest is to project the relative area of three bands in a ternary diagram, arbitrary referred as the ($B1$, $B2$, $B3$) triplet in the next equation. Each point on the diagram thus has coordinates

$$\{A_{Bi}/(A_{B1}+A_{B2}+A_{B3})\}_{i\in\{1,2,3\}} \quad (1)$$

where A_{Bi} is the area of Bi (Fig. 3). Working on relative areas is mandatory to compare spectra measured in different conditions of illumination and to remove the contribution of a potential dark absorbent. As altered/hydrous mineral spectra generally have three or more absorption bands, our approach is based on the projection of band areas into complementary selected spaces. We thus use four ternary diagrams combining six spectral variables selected according to the mineralogical endmembers seen in Jezero, in a so-called Triforce diagram: the areas

Table 1
List of the studied spectral ranges and the detection limits applied to each feature, in terms of band depth (BD) and band depth-to-noise ratio (BDNR, see Section 2.5). The number of Gaussians used to model each band is also indicated. BDNR stands for band depth-to-noise ratio.

Spectral feature	Wavelength range (μm)	BD thres. (%)	BDNR thres.	Nb. of Gaussians
B1400	1.356–1.513	2	2	2
B1900	1.808–2.170	2.1	9	4
B2200	2.102–2.305	2.5	7	2
B2300	2.221–2.396	2	5	3
B2500	2.379–2.580	2.7	7	2
S_INDEX[a]	2.115–2.405	2	10	N/A
1.3 - 1.8 μm slope	1.314–1.800	N/A	N/A	N/A

[a] Adapted from Viviano et al. (2014): S_INDEX = $1 - \frac{a\,R2115 + b\,R2405}{R2289}$.

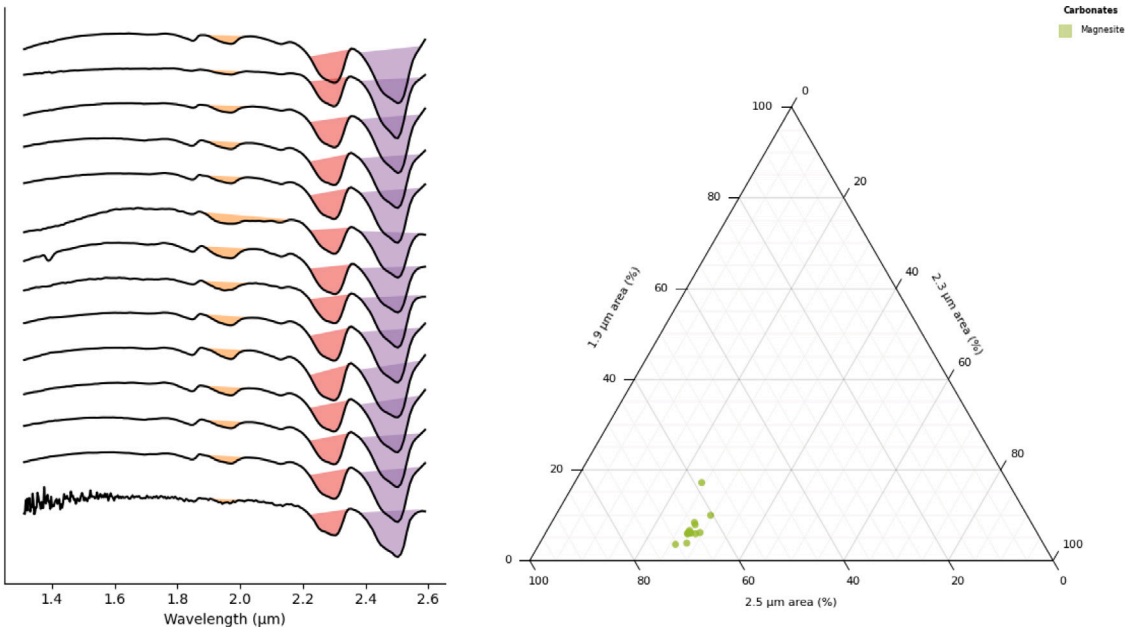

Fig. 3. Illustration of the MultiGM ternary projection. Left: near-IR spectra of different samples of magnesite (c1jb946a, c1jb946b, c1jb946c, c1jb946d, c1jb946e, c1sh02, c1sh03, c1sh19, c2jb946a, c2jb946b, cacb06, cacb70, cbcb06 – RELAB Database. Colored areas correspond to the automatically extracted areas of 1.9, 2.3 and 2.5 μm bands. Right: projection of relative areas in a ternary diagram (green points). (For interpretation of the references to color in this figure legend, the reader is referred to the web version of this article.)

of the bands at 1.4 (OH), 1.9 (H_2O), 2.2 (Si/Al-OH), 2.3 (Fe/Mg-OH or CO_3) and 2.5 μm (CO_3), plus the sulfur index (S_INDEX) measuring the spectral downturn at 2.3 – 2.4 μm and the 1.3 – 1.8 μm slope characterizing the long wavelength shoulder of the 1 μm band of Fe^{2+}-bearing mineral. These last two variables are not a band area, but they do help discriminate sulfates and olivines from other common minerals. The Triforce diagram with all six indices will be shown in next section.

2.3. Application laboratory spectra

We first apply this approach to a series of laboratory spectra re-sampled and convolved to IRS spectral response. Fig. 4 shows the distribution of zones for common mineral families, in the context of the aqueous alteration of a rocky surface. Each patch represents the area enclosing the measured relative band area projected in the given ternary diagram.

The various mineral families occupy distinct positions within each diagram. Fe/Mg-phyllosilicates are primarily characterized by their absorption bands at 1.4, 1.9, and 2.3 μm, associated with the hydration and hydroxylation of Fe and Mg. Serpentines are differentiated from smectites by the presence of a weak band at 2.5 μm, leading to the formation of two distinct clusters in Fig. 4B. Although carbonates do not contain OH or H_2O in their mineral structure, most of available laboratory spectra of those minerals exhibit a 1.9 μm band due to adsorbed water. In order to only represent the position of non hydrated carbonates in the Triforce diagram, the measurement of the 1.9 μm band area has been set to 0. Hydrated ones and mixtures with Fe/Mg-clays would follow the gray arrow drawn in (Fig. 4B). The same process is applied to kaolinite and serpentine for the same reason, (Fig. 4C). Siderite displays a strong absorption at 1 μm related to Fe^{2+}, similar to that of olivine, enabling the separation of Fe-rich carbonates or mixtures containing olivine from those dominated by Fe/Mg-phyllosilicates (Fig. 4A). Some hydrated phases may also exhibit a 2.5 μm band attributed to H_2O or OH, such as serpentines, Fe-hydroxides, but the other bands' relative area are sufficiently different to make them distinguishable from carbonates in Triforce diagrams (see Fig. 4B).

Alteration phases containing Al or Si hydroxides are characterized by the presence of an absorption band at 2.2 μm absent in all others. Therefore, projecting observations onto a 1.4 μm – 1.9 μm – 2.2 μm diagram effectively separates them (Fig. 4C). Furthermore, the relatively lower intensity 2.2 μm band areas are associated with hydrated silica (opal-A, chalcedony, hydrated glass) compared to relatively higher intensity band areas for Al-rich smectite (montmorillonite, illite), kaolinite/halloysite, and Al hydroxide (boehmite, gibbsite).

In the near-IR, sulfates are characterized by a drop in reflectance at 2.4 μm, measurable using the sulfur index (S_INDEX, named after Viviano et al. 2014 spectral parameter, even if this feature is attributed to H_2O), which is anticorrelated with the 2.3 μm band. Thus, a 1.9 μm – 2.5 μm – S_INDEX diagram effectively isolates sulfate-rich phases from Fe/Mg smectites and carbonates (Fig. 4D). However, the presence of a 2.2 μm band may lead to an increase in S_INDEX, potentially

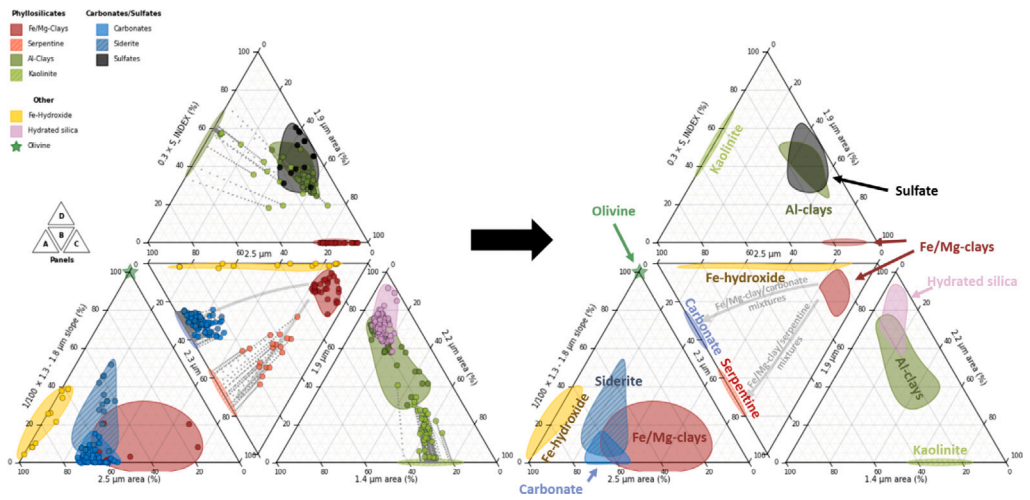

Fig. 4. Triforce ternary representation populated with terrestrial mineral samples measured in laboratory. The relative weight of the 1.3–1.8 μm slope and the S_INDEX is reduced to better distribute the points across the diagrams. In the inner triangle, the 'area' is omitted in the axes labeling due to space limitation. (Left) Colored points are the projections of laboratory spectra. Gray dotted lines correspond to the trajectory of carbonate-, serpentine- and kaolinite-bearing points when the 1.9 μm band area trends to zero. The ellipses on the 1.9 μm area = 0 axis are those minerals' asymptotic locations. (Right) Triforce diagram used in subsequent figures representing the laboratory spectra positions as patches. Species that do not contain water in their chemical formula are represented at their asymptotic position, when the 1.9 μm band area tends to zero. The gray arrows are the trends followed by nontronite/carbonate and nontronite/serpentine mixtures in various proportions.

confusing the spectral mixture interpretation. Therefore, it is necessary to compare this diagram with the 1.4 μm – 1.9 μm – 2.2 μm diagram to establish the presence of sulfates in the mixture.

Of note, the spectra used to populate the Triforce diagram are from terrestrial spectral libraries (RELAB, USGS) and even after careful the selection of the purest and least hydrated spectra, spectra acquired in Martian analog conditions are not always available. This may result in a potential bias in the position of the mineral patches in the diagram along the 1.9 μm direction.

The list of laboratory spectra used to populate Fig. 4 is provided in Supplementary Information (CSV sheet containing RELAB and USGS Database mineral names in each mineral family).

2.4. Advantages and limitations

The main advantage of the MultiGM representation of absorption bands is that it enables precise assessment of the band center for each bin defined in Table 1, and the projection into the Triforce diagram offers rapid visualization of the data and provides insights about the nature of the major mineral phases composing the targets studied, especially if additional information is encoded in the diagram (quality of detections, geological units of origin, grain size of targets, etc. See diagrams in Section 3). In addition, the combination of the projections enables mineral families to be separated more effectively. For example, sulfates and Al-phyllosilicates are positioned in the same place in the ternary diagram 1.9 μm – 2.5 μm – S_INDEX, whereas only Al-phyllosilicates are visible in the diagram 1.4 μm – 1.9 μm – 2.2 μm. Finally, simple mineral mixtures (of two or three main components) are easily separated as their points in the diagrams draw trends between laboratory reference areas.

However, the main limitation of this representation comes with complex mineral mixtures. In this case, the points describing the measured targets are found at an average position, not particularly close to a laboratory reference zone, or at the intersection of several zones (spectral library minerals are often impure and diverse). Another major limitation of the method is that it cannot account for the presence of minerals showing none of the plotted spectral characteristics, such as spectrally flat phases (plagioclase feldspars, most iron oxides, anhydrous/non hydroxylated substances, except carbonates) or minerals with broad absorption bands, which may merge with those of other minerals, such as olivines and pyroxenes. For these particular minerals, comparison with other methods such as spectral deconvolution and/or techniques such as the laser-induced breakdown spectroscopy (LIBS) or the Raman spectroscopy become necessary.

2.5. How to read a Triforce diagram?

A Triforce diagram, as depicted in Fig. 4, is a combination of four ternary diagrams, with adjacent axes representing the same spectral parameter. Each ternary is labeled A, B, C, or D according to its position in the diagram (see the schematic on the left of each diagram), and each represents the projection of the relative intensity of three spectral parameters (band area, S_INDEX, or 1.3–1.8 μm slope).

- Ternary A corresponds to the projection 1.3–1.8 μm slope – 2.3 μm – 2.5 μm, enabling discrimination of phases exhibiting an absorption related to Fe^{2+} around 1 μm, such as olivine and Fe-bearing carbonates. The 1.3–1.8 μm slope parameter has been diminished by a factor of 100 to better spread the points in the diagram.
- Ternary B corresponds to the projection 1.9 μm – 2.3 μm – 2.5 μm, allowing discrimination between Fe/Mg-smectites (lacking a band at 2.5 μm) and carbonates and serpentines. It is noteworthy that mixtures of carbonates and smectites are distinguishable from smectite/serpentine mixtures as they follow a trajectory represented by the gray arrow, well separated from the region covered by serpentines.
- Ternary C corresponds to the projection 1.4 μm – 1.9 μm – 2.2 μm, facilitating the study of mixtures containing phases with an absorption at 2.2 μm (Si/Al-OH) such as Al-smectites, kaolinite, Al-OH, and hydrated silica.
- Ternary D corresponds to the projection 1.9 μm – 2.5 μm – S_INDEX, allowing the study of mixtures positively responding to S_INDEX, thus containing sulfates. The presence of a band at 2.2 μm leads to a false positive for this spectral parameter, so the ternary must be read jointly with ternary C to discriminate between a mixture containing sulfates and one containing Si/Al-OH. The S_INDEX parameter has been diminished by a factor of 0.3 to better spread the points in the diagram.

Observations from IRS/SuperCam are projected onto the Triforce diagram as points of different sizes and colors. The color of the points represents the geological unit to which the observed rock belongs,

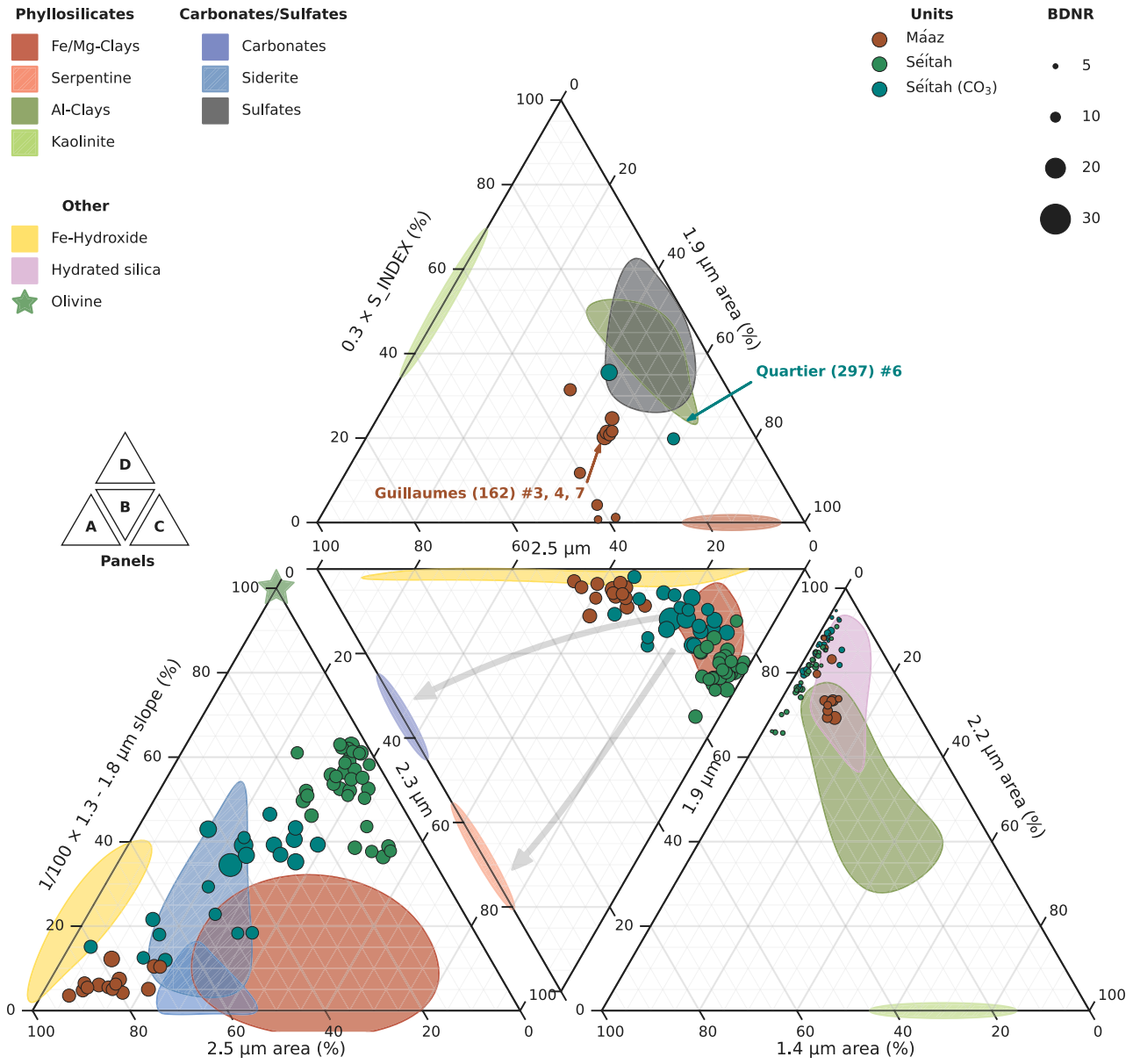

Fig. 5. Crater floor Triforce plot. The projection of surfaces and relative band parameters for all targets belonging to the Crater floor units is illustrated. The point size corresponds to the combination of band depth-to-noise ratios of the bands involved in each ternary diagram: the larger the point, the higher the quality of detection. Colors indicate the geological units where the targets were measured, filtered by quality: lower quality measurements are shaded to enhance the depiction of clusters and trends. Refer to Fig. 4 for a description of the diagram background (axes, patches, and arrow). The observations of the Quartier and Guillaumes abrasion patches are highlighted in Ternary D to show the occurrence of sulfates. (For interpretation of the references to color in this figure legend, the reader is referred to the web version of this article.)

while the size corresponds to the quality of the triplet of spectral parameters. This quality is the combination of the three band depth-to-noise ratios calculated from the uncertainty of the data and the band depth. The uncertainty of the band depth (BD) is estimated using the uncertainties (σ) of the three points used to calculate it, *i.e.*, the band minimum and its two shoulders, in reflectance (R). It is determined by considering the errors of these three points as independent, which is justified by the fact that the IRS acquires the spectral channels successively by changing the state of its AOTF filter. The band depth to noise ratio (BDNR) is then calculated by:

$$\mathrm{BDNR} = \mathrm{BD} \times \left[(1 - \mathrm{BD}) \left(\frac{\sigma_c^2}{R_c^2} + a^2 \frac{\sigma_s^2}{R_s^2} + b^2 \frac{\sigma_l^2}{R_l^2} \right) \right] \quad (2)$$

Where a and b are weighting coefficients corresponding to the relative distance between the band minimum and the shoulders, and the c, l and s subscripts correspond to the position of the band minimum (or center) and the short and long wavelength shoulders (see Viviano et al. 2014). Reflectance and uncertainty are provided for each observation by the SuperCam Bundle on the NASA Planetary Data System (Maurice et al., 2021).

The position of the points in the different triangles indicates the dominant mineral family in the target's spectrum, but a more precise identification of the minerals requires studying the distribution of the absorption band positions (plotted in this study along with Triforce diagrams). In the case of IRS/SuperCam, the attribution of spectral features to a specific mineral species is also supported by the rover's other instruments.

3. Mineral diversity across Jezero crater floor and western fan

3.1. Dataset description

In this study, we applied the method previously described to the entire dataset acquired by the IRS instrument from landing to Sol ~

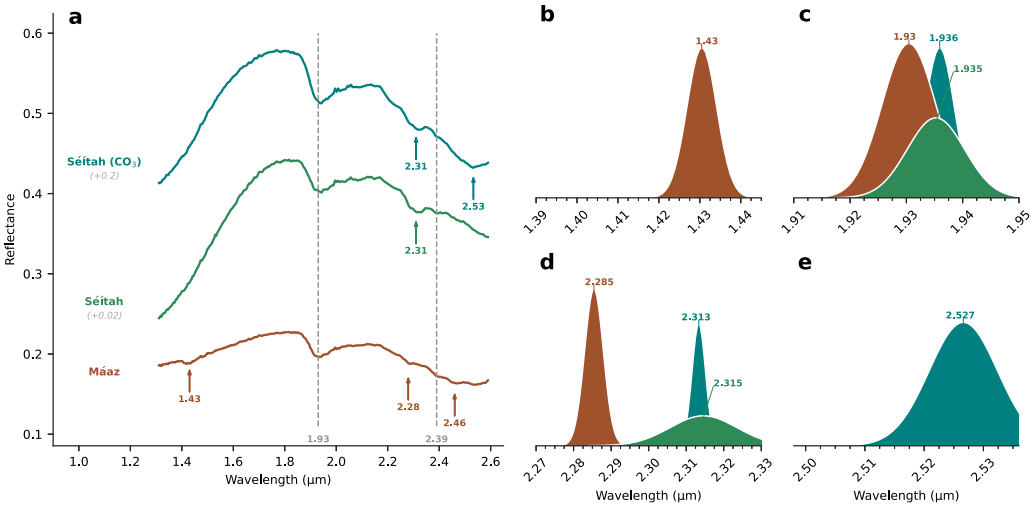

Fig. 6. a: Average spectra of the identified clusters in the Triforce plot (Fig. 5). The positions of the main absorption bands are indicated, using arrows for specific cases or dashed lines for bands common across spectra. The gray number in parentheses represents the offset added to the reflectance for clarity. b – e: Histograms depicting the positions of absorption bands (1.4 μm: b; 1.9 μm: c; 2.3 μm: d; 2.5 μm: e) for targets within each cluster, adjusted by a Gaussian curve to enhance the visualization of differences between units. The mean of each distribution is indicated.

1100, with the exception of soil, regolith, and float rock observations (unless specified), as these do not a priori exhibit a clear link with local stratigraphy. We also removed all spurious observations: affected by instrument artifacts, shadowed, masked by rover's hardware. For projection onto Triforce diagrams (Figs. 5, 7, 9, 11), an additional filter is applied: only spectra featuring significant absorption bands (in terms of depth and band depth-to-noise ratio, see Table 1) are represented. Indeed, when only weak bands are present, a slight relative variation in their surface (due to noise, for example) can lead to a broad spread of points in the diagram, thereby distorting its interpretation. Subsequently, we examine the statistical distribution of band positions in these spectra to identify dominant mineral phases. The spectra depicted in Figs. 6, 8, 10, 12 thus do not represent the average spectra of geological units, but rather the average of spectra featuring the most intense absorption bands. In total, 41% of the whole dataset is represented in this analysis (2761 spectra).

3.2. The Crater floor

The Crater floor is the igneous floor of Jezero crater (Farley et al., 2022) below the delta/fan structure (Paige et al., 2022). It comprises two main geological units: Máaz, effusive volcanic lava flows forming the majority of the Crater floor, and Séítah, a local topographic rise consisting of layered olivine cumulates covered with sand dunes and stratigraphically below Máaz (Farley et al., 2022; Maki et al., 2023).

The projection of spectral parameters calculated from IR measurements conducted in the Crater floor onto the Triforce diagram reveals a prevailing composition dominated by Fe/Mg-smectites (*e.g.*, saponite and nontronite) as an alteration phase (Fig. 5B). However, marked differences among regional units emerge, displaying well-defined clusters when focusing on observations with the best band depth-to-noise ratio (Fig. 6): Máaz includes hydrated phases but appears relatively unaltered, as revealed by the distribution of the points with high 1.9 μm band area (Figs. 5B, 5D), lower 2.3 μm band relative weight (Fig. 5B), nearly absent 2.2 μm band (Fig. 5C), and weak response to the S_INDEX (Fig. 5D). The apparent strength of the 2.5 μm band in these rocks is likely related to a residual instrument radiometric calibration, leading to a relative overestimation of this band when others are weak (see Royer et al. 2023) or to some Fe-oxyhydroxides. The modeled band position using MultiGM shows that the 2.3 μm band is actually located at 2.28 μm, attributable to Fe-OH, marking a clear difference with the other units (Fig. 6d). More precisely, Máaz spectra exhibit a combination of 1.43 and 2.28 μm bands (Fig. 6b and d) as well as a weak 2.39 μm absorption (Fig. 6a) indicative of the presence of Fe-OH in phyllosilicates.

Measurements in Séítah exhibit greater diversity, clustering into two main groups, both dominated by the very prominent 1.3 – 1.8 μm slope attributed to olivine (Fig. 5A). The first one has a nearly absent 2.5 μm band (in green in Figs. 5 and 6) and the second contains targets exhibiting stronger 2.5 μm band, representing the onset of a minor clay-carbonate mixture trend (Fig. 5B) and a cluster in the siderite area in Fig. 5A diagram (labeled Séítah (CO_3) in Fig. 5 and Fig. 6). This second group of rocks is likely more altered, containing mixtures of olivine, Fe/Mg-smectites (2.31 and 2.39 μm bands, Fig. 6a, d), and Fe-bearing carbonates (2.31 and 2.53 μm bands, Fig. 6a, d, e). A weak 2.2 μm band (Al/Si-OH) is visible in averaged spectra but too weak to have its position clearly measured. The 1.93-94 μm band of those targets is indicative of the presence of Fe-oxyhydroxide (Fig. 6c) shifting this band's position toward longer wavelengths. Notably absent in Séítah are the 2.2 μm band and sulfates, except in the Quartier abrasion patch, observed on Sol 297, where sulfates were observed (Fig. 5D).

3.3. The Shenandoah formation

The Shenandoah formation encompasses all units explored by the rover during the Delta Front Campaign, distributed across the two lobes visited by Perseverance: Cape Nukshak and Hawksbill Gap, situated west and north of Three Forks, respectively (Fig. 1). While the complexity of sedimentary delta deposition mechanisms prevents an exact correspondence of strata at identical elevations in both lobes, the projection of measurements in the Triforce diagram indicates the presence of three main clusters and similarities between certain units in Cape Nukshak and Hawksbill Gap (Fig. 7).

The Amalik member forms its distinct group due to its unique signature at 2.32 μm (Fig. 8d) associated with Mg-serpentine, along with the 1.41 μm band predominantly linked to Mg-OH. Additionally, it exhibits a weak absorption band at 2.52 μm attributed to H_2O (Fig. 8e). Carbonates are unlikely as this cluster does not plot in the carbonates area or along the Fe/Mg-smectites – carbonates trend.

The cluster consisting of the Devils Tanyard, Knife Creek, and Hughes River Gap members (Fig. 7) exhibits characteristic signatures of Fe/Mg-smectites (bands at 1.42–43, 2.31, and 2.39 μm associated with Fe-OH, Fig. 8a, b, d) and vermiculite (doublet at 2.3 μm, see Swayze et al. 2018), with minimal to no 2.5 μm band presence.

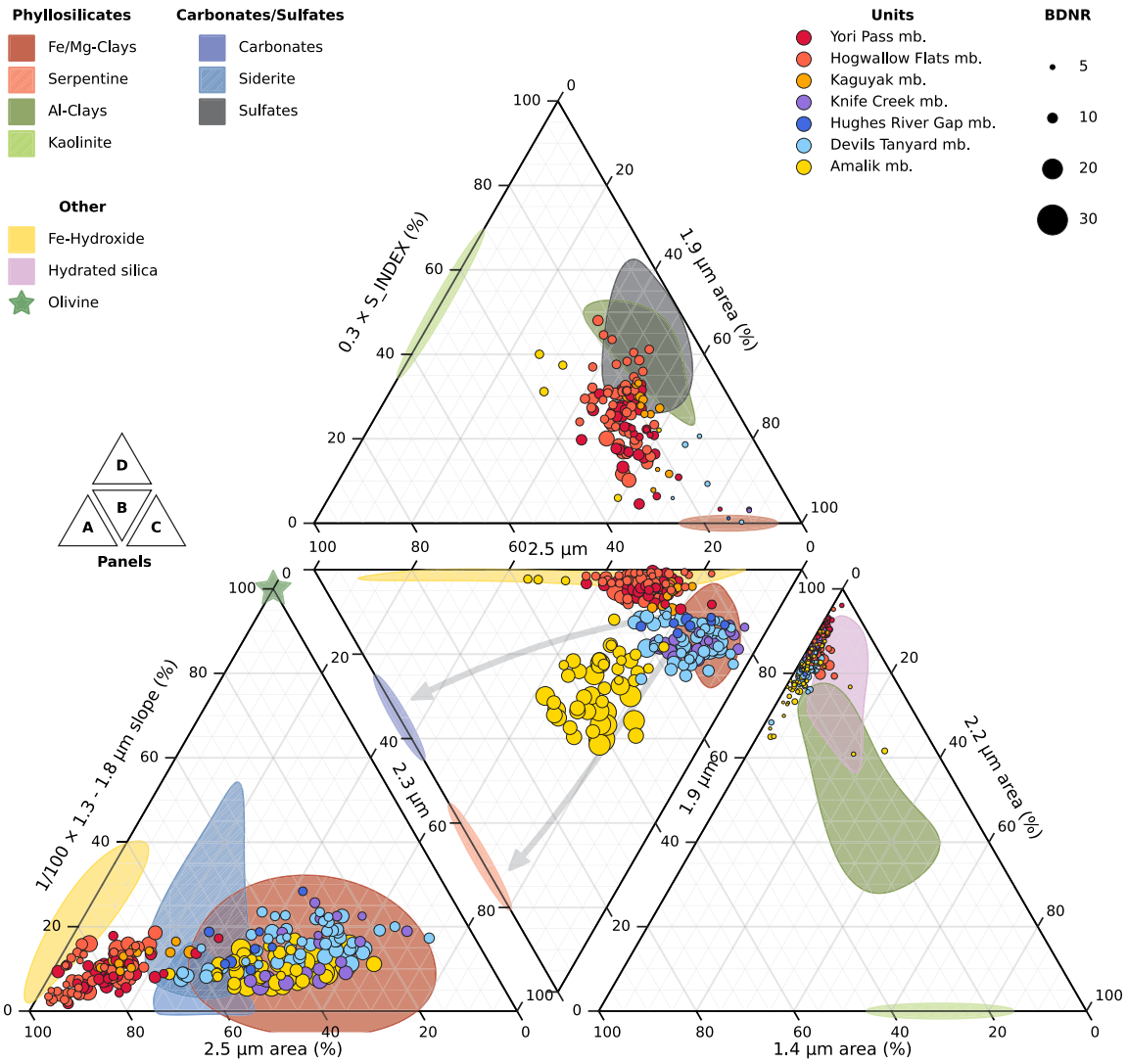

Fig. 7. Shenandoah formation Triforce plot. The projection of surfaces and relative band parameters for all targets belonging to the Shenandoah formation's units is illustrated. The point size corresponds to the combination of band depth-to-noise ratios of the bands involved in each ternary diagram: the larger the point, the higher the quality of detection. Colors indicate the geological units where the targets were measured, filtered by quality: lower quality measurements are shaded to enhance the depiction of clusters and trends. Refer to Fig. 4 for a description of the diagram background (axes, patches, and arrow). (For interpretation of the references to color in this figure legend, the reader is referred to the web version of this article.)

Lastly, the cluster containing the Hogwallow Flats, Yori Pass, Kaguyak, and to a lesser extent Alagnak members forms a notable cluster in Fig. 7D, indicative of sulfate presence (lack of a 2.2 µm band indicating Al/Si-OH bonding, potentially biasing the S_INDEX). This cluster exhibits variable contributions of the 2.4 µm signature, reflected in its spread (Fig. 7D). Analysis of absorption band positions (Fig. 8) also reveals a shift towards longer wavelengths for the 1.4 µm (1.43–44 associated with Fe-OH and H_2O) and 1.9 µm bands (1.94 µm potentially affected by the presence of Fe-hydroxide and/or Mg-sulfates), while the 2.29-30 µm band suggests a composition of smectites richer in Fe. Lastly, these targets exhibit a notable 2.5 µm band (Fig. 8e) at 2.52-53 µm that can be attributed to H_2O or to Fe/Ca-rich carbonates although the characteristic 1.3 – 1.8 µm slope indicative of Fe^{2+} in siderite (Gaffey, 1987) is absent. The position of the points in the Triforce diagram (Fig. 7) favors H_2O over CO_3 for this feature.

3.4. The Tenby formation

The Tenby formation represents the stratigraphic stage just above the Shenandoah formation and constitutes the upper part of the delta/fan (Fig. 1). It encompasses three main geological units visited by Perseverance: Rockytop (subdivided into "lower" and "upper"), Skrinkle Haven, and Carew Castle. The upper fan also includes rocky boulders seemingly unrelated to the stratigraphy, with compositions notably different from the bedrock. The boulder units most extensively documented by SuperCam in this study are Falcon Lake and Mount Meeker both observed near Sol 850 (Dehouck et al., 2024; Beyssac et al., 2024).

The projection of spectral parameters from units within the Tenby formation onto the Triforce plot delineates three distinct clusters (Fig. 9). The Rockytop members exhibit a similar composition characterized by a moderate response to S_INDEX and the absence of the 2.2 µm band, while the average spectrum shows no sharp drop in reflectance at 2.4 µm, as observed in Hogwallow Flats or Yori Pass (Fig. 10). Instead, this response is due to the lowering of the right shoulder of the 1.9 µm band, leading to an increased separation between the center of the criterion (2.30 µm, Table 1) and its edges (2.12 and 2.40 µm). This reflectance decrease can be attributed to the broadening of the 1.9 µm band related to the presence of polyhydrated Fe or Mg-sulfates. This observation is also consistent with the shift towards a longer wavelength center of the 1.9 µm signature in comparison to phyllosilicate-rich endmembers. Additionally, the average spectrum of

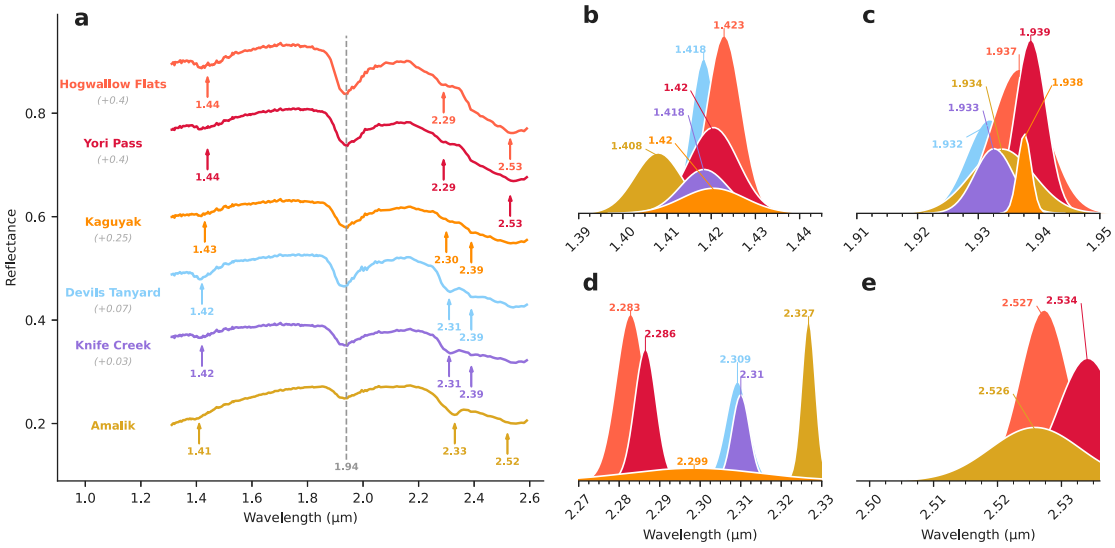

Fig. 8. a: Average spectra of the identified clusters in the Triforce plot (Fig. 7). The positions of the main absorption bands are indicated, using arrows for specific cases or dashed lines for bands common across spectra. The gray number in parentheses represents the offset added to the reflectance for clarity. b – e: Histograms depicting the positions of absorption bands (1.4 μm: b; 1.9 μm: c; 2.3 μm: d; 2.5 μm: e) for targets within each cluster, adjusted by a Gaussian curve to enhance the visualization of differences between units. The mean of each distribution is indicated.

these rocks exhibits a strong 2.5 μm band but lacks a 2.3 μm band as observed in carbonates (Fig. 10). This lack of 2.3 μm feature can be explained by the presence of Mg-sulfate in intimate mixture leading to the masking of this feature (Sheppard et al., 2024). Alternatively, some zeolites could explain these spectral properties (Cloutis et al., 2002) but the lack or weak 1.4 μm signature does not support the presence of this mineral phase. However, the 2.5 μm band can still be attributed to H_2O in other minerals such as Fe-oxyhydroxides.

The Carew Castle and Skrinkle Haven members exhibit highly similar behavior in the Triforce plot (Fig. 9), forming a broad cluster in the phyllosilicates-carbonates mixing area and are characterized by a strong 1.3 – 1.8 μm slope attributed to olivine and/or Fe-bearing carbonate (Fig. 10). However, some Skrinkle Haven points appear more advanced along the Fe/Mg-smectite – carbonates trend (gray arrow in Fig. 9B) and closer to the magnesite/calcite pole than the siderite pole in Fig. 9A diagram. This property is visible in the analysis of band positions where Carew Castle spectra exhibit a longer-wavelength 2.5 μm band compared to Skrinkle Haven, signifying an enrichment in Mg (Fig. 10) (Beck et al., 2024b). Some Carew Castle points also deviate from the cluster by weakening the contribution of the 2.5 μm band and strengthening the 1.3–1.8 μm slope, indicating lower alteration. In addition, both members exhibit a 2.21-22 μm band attributable to Si-OH (Fig. 10c) and a weak 2.39 μm band attributable to Fe-OH in smectites.

Lastly, observations from the olivine-rich boulders (near Falcon Lake, Fig. 1) form a cluster similar to what was observed with Séítah (Fig. 5), exhibiting a strong 1.3 – 1.8 μm slope attributed to olivine, a weak 1.9 μm band compared to other units, and a 2.3 μm band shifted to 2.31-32 μm, suggesting serpentines (Fig. 9, Fig. 10). The other boulder group, the pyroxene-rich boulders (near Mount Meeker, Fig. 1), is not visible in the Triforce diagram projection as its spectra are predominantly marked by low calcium pyroxene feature (broad 2 μm band, Fig. 10a) and weak alteration (Dehouck et al., 2024). Only one point from Dragon's Egg Rock could appear on Fig. 9, it corresponds to an anhydrite vein unveiled by the abrasion by the rover. Anhydrite has no water in its crystalline structure, it is thus not visible in the 1.3–2.6 μm range. But it can contain residual water, in the form of bassanite, which is responsible for the presence of typical 1.4, 1.9 and 2.4 μm features (Cloutis et al., 2007, 2008; Poitras et al., 2018).

3.5. The Margin unit

The Margin unit is located west of and at slightly higher elevation than the delta top, extending from the crater rim to the most westward channels carved into the delta (Fig. 1). It extends both north and south of Neretva Vallis. Its differentiation from the Tenby formation is primarily due to its geomorphological features and orbital spectral characteristics measured in the near-IR by MRO/CRISM. Indeed, this regional unit encompasses the most significant and abundant spectral signatures associated with carbonates (absorption bands at 2.3 and 2.5 μm) (Goudge et al., 2015b; Horgan et al., 2020; Brown et al., 2020; Zastrow and Glotch, 2021; Tarnas et al., 2021). The rover's exploration of this unit is ongoing at the time of the writing, therefore the attribution of the observations to the units may vary in the future. Here we group the targets by location rather than stratigraphic members. Our groups include Hans Amundsen Memorial Station (Fig. 1), where *Perseverance* first entered the Margin unit, Turquoise Bay, slightly farther north, Bernier Island, in between the latter two and along the westernmost river channel, Airey Hill/Gnaraloo Bay, east of Jurabi Point, and Bunsen Peak at the western end of the investigation area. Some rocks are not clearly linked to a unit and are gathered under 'Miscellaneous margin' in Fig. 11. These rocks correspond to the region between Jurabi Point and Bunsen Peak (Fig. 1).

The Triforce projection of SuperCam spectral parameters does not clearly distinguish well-defined clusters, instead, the observations form a continuum of Fe/Mg-phyllosilicates – carbonate mixtures showing a variable enrichment in carbonates (Fig. 11B). The mean spectra of all units exhibit similar absorption bands: 1 μm (Fe^{2+}) as suggested by the 1.3 – 1.8 μm slope, 1.93–94 (OH in hydroxides and/or sulfates), 2.21 (Si-OH), 2.31 (Fe/Mg-OH and CO_3), 2.39 (Fe-OH in phyllosilicates), and 2.52-53 μm (CO_3 in ferrous carbonates) (Fig. 12a). However, local differences are visible.

The rocks from Hans Amundsen (H. A.) Memorial and Bernier Island cluster around the patch of Fe/Mg smectite-rich mixtures (Fig. 11B), but some points appear to stand out and form a trend between the siderite zone and altered olivine (Fig. 11A). These points correspond to measurements taken on the Amherst Point abrasion patch on Sols 922 and 925. Their position in the diagram indicates a relative strengthening of the slope between 1.3 and 1.8 μm, attributable to reduced dust impact and/or the presence of larger olivine or Fe-bearing carbonate grains within the rock. The distribution of the absorption band positions

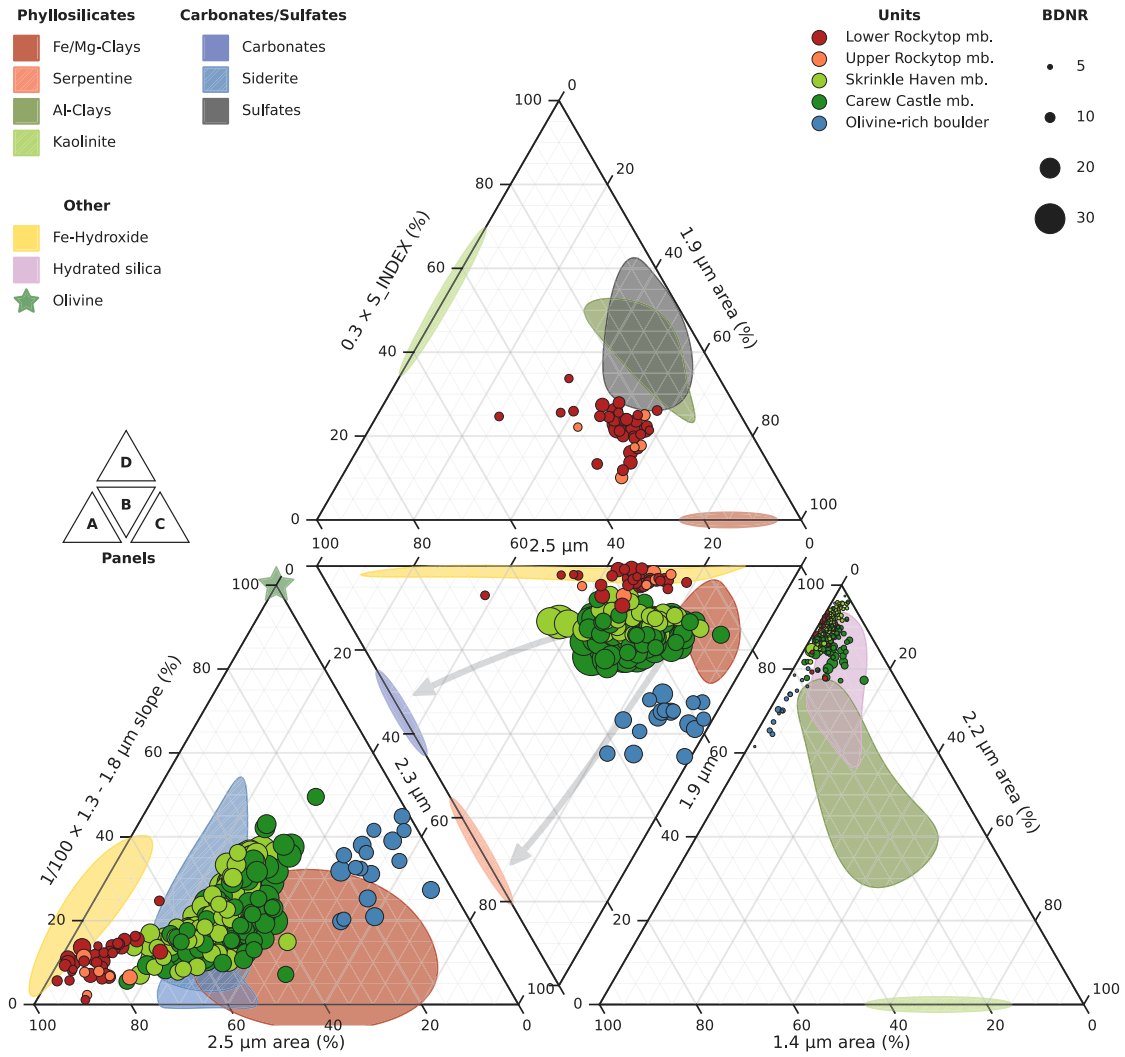

Fig. 9. Tenby formation Triforce plot. The projection of surfaces and relative band parameters for all targets belonging to the Tenby formation's units is illustrated. The point size corresponds to the combination of band depth-to-noise ratios of the bands involved in each ternary diagram: the larger the point, the higher the quality of detection. Colors indicate the geological units where the targets were measured, filtered by quality: lower quality measurements are shaded to enhance the depiction of clusters and trends. Refer to Fig. 4 for a description of the diagram background (axes, patches, and arrow). (For interpretation of the references to color in this figure legend, the reader is referred to the web version of this article.)

also agrees with mixtures of clays, carbonates, and hydrated silica (band at 2.22 µm). The distribution of the 2.3 µm band appears bimodal (Fig. 12d), with some occurrences of absorptions at 2.29 µm parallel to the more numerous ones at 2.31 µm. This would indicate variable mixtures of Fe and Mg in phyllosilicates, in combination with ferrous carbonates (band at 2.53 µm, Fig. 12e).

Turquoise Bay, Airey Hill and Gnaraloo Bay exhibit similar spectral characteristics to the H. A. Memorial but with a pronounced enhancement of carbonate presence. Measurements in those units extend further towards the carbonate area (Fig. 11B), and the 2.5 µm band is deeper in the mean spectra (Fig. 12a). The position of this band is also shifted towards shorter wavelengths (2.52 µm, Fig. 12e) and weakly bimodal (some occurrences of the band at 2.50 µm in Turquoise Bay), indicating an enrichment in Mg carbonates with some occurrences particularly enriched in Mg.

Bunsen Peak is a rocky prominence of the Margin unit, exhibiting spectral characteristics that differ from previously visited units. Its spectral enrichment in carbonates is the strongest ever observed, and the mean position of this band (2.52 µm, Fig. 12e) indicates a higher average concentration of Mg-carbonate among the Margin units. Additionally, it presents a prominent band at 2.31 µm, consistent with Fe/Mg-smectites and/or carbonates (Fig. 12d), and a band at 2.22 µm attributable to hydrated silica (Fig. 12c).

Finally, observations of the misc. Margin unit targets along the main westward traverse in the margin unit (Fig. 1) tend to resemble nearby Bunsen Peak in terms of absorption bands, band positions, and depths.

4. Discussion

4.1. List of the secondary phases identified by the model

The spectral analyses of the IRS data collection support the presence of mineral phases or specific mineral species. Table 2 lists the major minerals families identified in the various Jezero units. In the next section, we discuss the local variations of these phases for each major unit.

4.2. Comparison between units and with other techniques

The entirety of the bedrock within the Jezero crater exhibit a significant diversity of spectral signatures in the near-IR, indicating their mineralogical diversity. However, the main absorption bands identified correspond to water (1.4, 1.9 µm), Fe^{2+} (1.3 – 1.8 µm slope), hydroxylation of Fe, Mg (2.28–2.33 µm, 2.39 µm), and to a lesser extent Si (2.22 µm), and $FeCO_3$ (2.53 µm). The automated

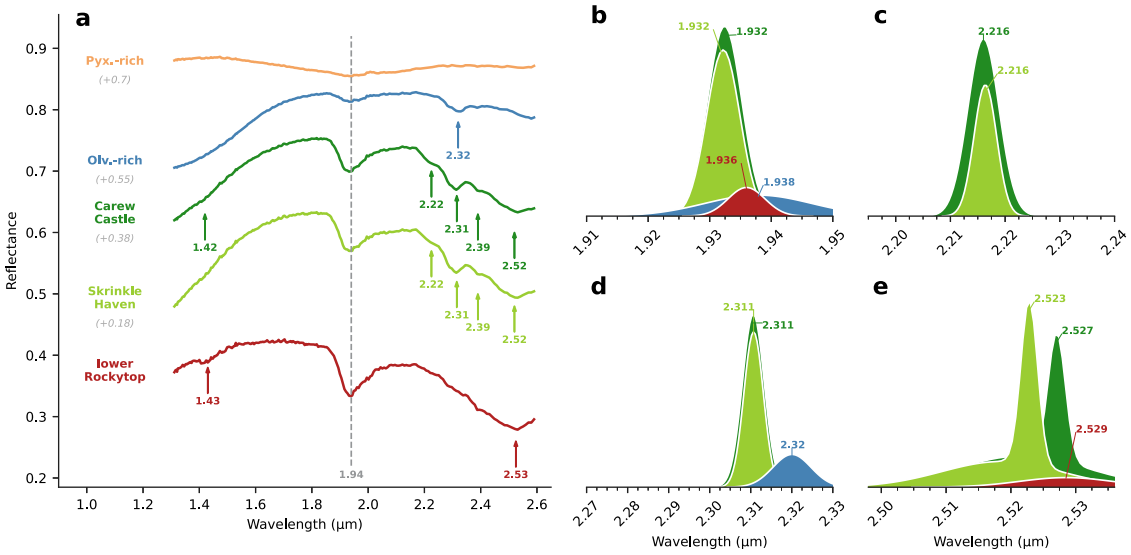

Fig. 10. a: Average spectra of the identified clusters in the Triforce plot (Fig. 9). Olv. = olivine, Pyx. = pyroxene. The positions of the main absorption bands are indicated, using arrows for specific cases or dashed lines for bands common across spectra. The gray number in parentheses represents the offset added to the reflectance for clarity. b – e: Histograms depicting the positions of absorption bands (1.9 μm: b; 2.2 μm: c; 2.3 μm: d; 2.5 μm: e) for targets within each cluster, adjusted by a Gaussian curve to enhance the visualization of differences between units. The mean of each distribution is indicated.

Table 2
Summary of identified mineral phases with the Triforce projection compared to band position distribution.

Regional area	Unit	Identified mineral phases	Comment
Crater floor	Máaz	Fe/Mg-smectite, sulfate	Dusty targets, smectites richer in Fe than Mg, sulfates in fracture fills
	Séítah	Fe/Mg-smectite, olivine, Fe-carbonate	Very prominent olivine signatures, quite scarce occurrences of carbonates
Shenandoah formation	Amalik/ Kaguyak	Mg-serpentine, Fe/Mg-smectite	
	Yori Pass/ Hogwallow Flats	Fe/Mg-sulfate, Ca-sulfate, Fe/Mg-smectite, Fe-carbonate	Strongest sulfate signatures
	Devils Tanyard/ Hughes River Gap	Fe/Mg-smectite, vermiculite	High spectral similarity with vermiculite
Tenby formation	Rockytop	Fe/Mg-sulfate, Fe/Mg-smectite, Fe-carbonate	Intimate mixture of Mg-sulfate and Fe-carbonate might mask carbonate 2.3 μm signature
	Carew Castle/ Skrinkle Haven	Fe/Mg-smectite, Fe/Mg-carbonate, hydrated silica	Various proportions of Fe and Mg in carbonates, overall richer in Fe
	Olivine-rich boulders	Olivine, Mg-serpentine, Fe/Mg-smectite	Poorly altered
	Pyroxene-rich boulders	Low calcium pyroxene, sulfates	Very poorly altered, sulfates in fracture fills
Margin unit	H. A. Memorial	Fe/Mg-smectite, Fe-carbonate, hydrated silica	Similar to Carew Castle and Skrinkle Haven, occurrences of Fe-rich smectites
	Turquoise Bay/ Airey Hill	Fe/Mg-smectite, Fe/Mg-carbonate, hydrated silica	Occurrences of very high Mg content in carbonates, occurrences of Fe-rich smectites
	Bunsen Peak	Fe/Mg-smectite, Fe/Mg-carbonate, hydrated silica	Variable Mg content in carbonates but overall greater than observed previously, stronger hydrated silica

extraction of absorption bands may contain certain biases such as false detections (mitigated by a more stringent detection threshold) and the poor estimation of band position when multiple bands overlap (*e.g.*, 2.30–2.33 μm region) or when the continuum cannot be accurately assessed, as in the case of the 2.5 μm band, due to the spectral range limitation of IRS. In the Crater floor, the detected absorption bands and their distribution are nevertheless consistent with previous works (Mandon et al., 2023), and also independent techniques for minerals such as olivine or carbonates (Clavé et al., 2023), confirming the feasibility of using the Triforce projection compared to band position distribution approach for automatic and systematic analysis.

The distribution of these spectral signatures along the rover traverse varies among geological units. Máaz appears to be igneous in nature with a chemical composition similar to that of calcium clinopyroxenes, such as diopside, and feldspars (Wiens et al., 2022; Udry et al., 2023). Its high Fe content (~ 18 wt%) compared to Mg (~ 3 wt%) and

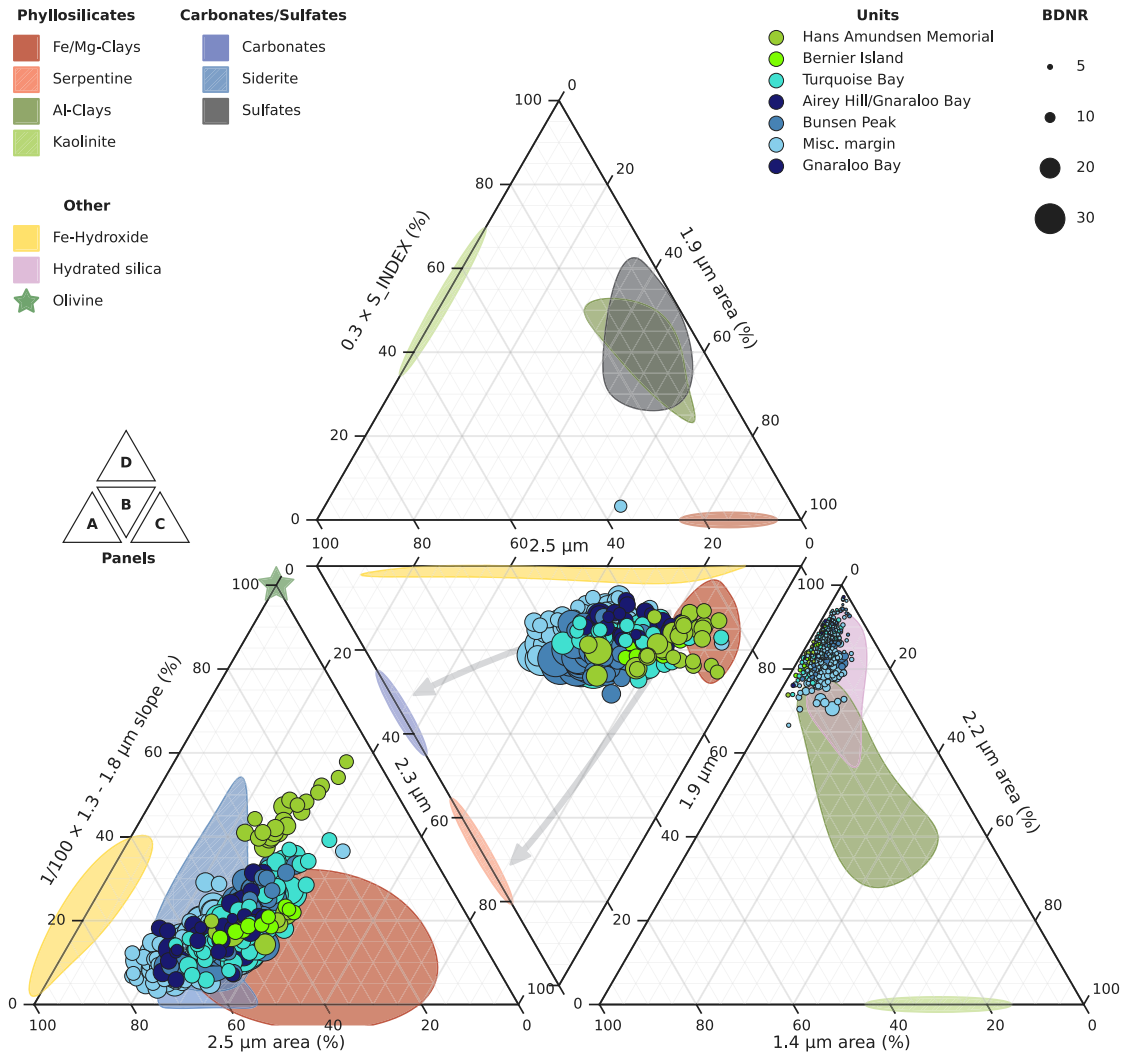

Fig. 11. Marginal unit Triforce plot. The projection of surfaces and relative band parameters for all targets belonging to the Tenby formation's units is illustrated. The point size corresponds to the combination of band depth-to-noise ratios of the bands involved in each ternary diagram: the larger the point, the higher the quality of detection. Colors indicate the geological units where the targets were measured, filtered by quality: lower quality measurements are shaded to enhance the depiction of clusters and trends. Refer to Fig. 4 for a description of the diagram background (axes, patches, and arrow). Misc. margin = miscellaneous units of the margin not attributed to a geological formation (work in progress).

alkali elements (~ 9 wt%) is consistent with the previously identified absorption bands (1.43, 2.28, and 2.39 µm) and proposed mineral assemblages (Fe/Mg-smectites, potential sulfates), suggesting that the alteration phases detected by the IRS originate from this primary pyroxene-rich composition. On the other hand, Séítah is a unit much richer in Fe and Mg (approximately 23 and 21 wt%, respectively) and depleted in alkali elements (~ 5.5 wt%), resembling an ultramafic composition, which, coupled with its apparent stratification and fine-scale texture, suggests it is an olivine-rich cumulate (Wiens et al., 2022; Liu et al., 2022; Beyssac et al., 2023). The alteration phases identified with the IRS here also support local aqueous alteration of an olivine-rich substrate (presence of Fe/Mg-smectites richer in Mg than for Máaz, Fe-carbonates), albeit brief enough in duration not to entirely alter the olivine (as evidenced by the persistent slope < 1.8 µm and detections by LIBS and Raman techniques). The carbonates detected with the IRS and the Triforce projection method correspond to the more ferrous end-member (band centered on 2.53 µm), which is inconsistent with the composition inferred from LIBS data (Mg concentration between 42 and 70%) by Clavé et al. (2023). However, two biases may include: (1) the radiometric calibration of IRS in the 2.5–2.6 µm range corrects an effect related to the temperature of the instrument's electronic board, leading to the appearance of a positive slope increase between 2.55 and 2.6 µm (see Royer et al. 2023). Despite calibration, a residual slope may remain, leading to an imprecise measurement of the position of the 2.5 µm band, especially when it is weak, as in Séítah; and (2) LIBS measurements on calibration targets on Mars show that the quantification of FeO content up to now tends to be underestimated (Wiens et al., 2022). The observation by PIXL on the Dourbes abrasion patch seems to confirm this underestimation trend by measuring a higher Fe content than with LIBS (Liu et al., 2022; Beyssac et al., 2023). The two sulfate detections in the Triforce plot (Fig. 5D) correspond to the Quartier (in Séítah) and Guillaumes (in Máaz) abrasion patches. The PIXL and SHERLOC instruments also detected these sulfates as local occurrences of veins or pore fillings by hydrated $MgSO_4$ (Siljeström et al., 2024).

In the Delta Front, Shenandoah formation, the spectra of the units notably differ from those of the Crater floor, exhibiting much deeper absorption bands related to aqueous alteration and the disappearance of signatures associated with primary minerals (1.3–1.8 µm slope). Two stratigraphic levels are clearly distinguished: the Amalik member with its absorption band at 2.33 µm attributed to Mg-rich serpentine, and the Hogwallow Flats, Yori Pass, and Rockytop units, forming a continuum around the delta, with their sulfate signatures. The presence of serpentine in Amalik suggests alteration in a weakly open system (perhaps a hydrothermal system), which is consistent with the Chemical

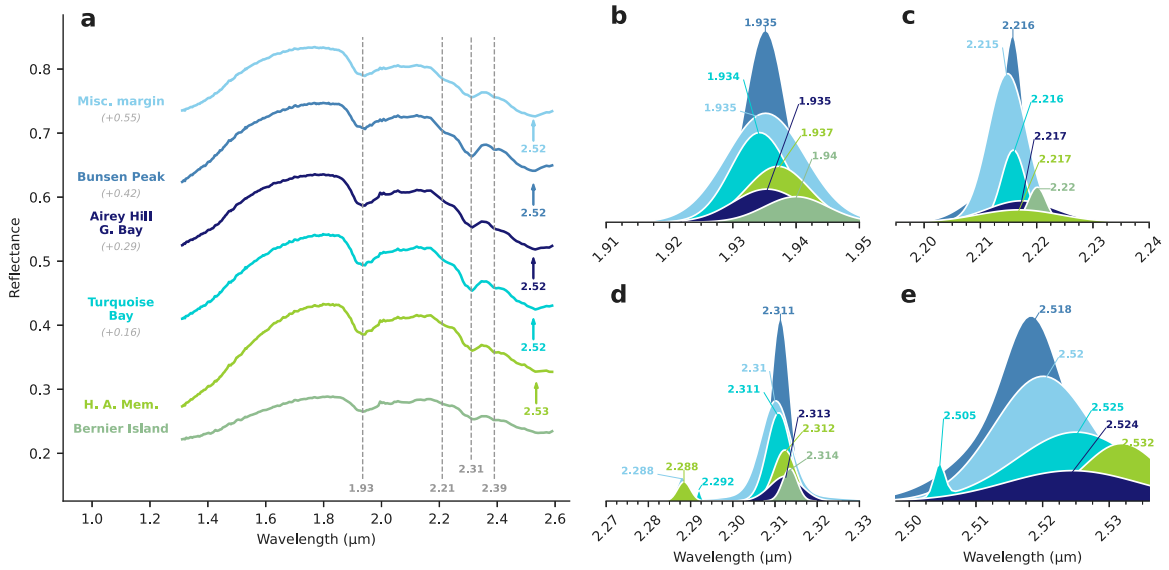

Fig. 12. a: Average spectra of the identified clusters in the Triforce plot (Fig. 11). The positions of the main absorption bands are indicated, using arrows for specific cases or dashed lines for bands common across spectra. The gray number in parentheses represents the offset added to the reflectance for clarity. b – e: Histograms depicting the positions of absorption bands (1.9 μm: b; 2.2 μm: c; 2.3 μm: d; 2.5 μm: e) for targets within each cluster, adjusted by a Gaussian curve to enhance the visualization of differences between units. The mean of each distribution is indicated. H. A. Mem. = Hans Amundsen Memorial, G. Bay = Gnaraloo Bay, Misc. margin = miscellaneous units of the margin not attributed to a geological formation (work in progress).

Index of Alteration (CIA) measurement of approximately 35% (Dehouck et al., 2023) using LIBS. The PIXL instrument does not formally detect serpentine but suggests the presence of Fe-enriched carbonates (ferrodolomite) (Hurowitz et al., 2023) which would be compatible with the weak 2.52 μm band visible in the average IRS spectrum. PIXL analysis of the Novarupta abrasion patch suggests the presence of small olivine grains (Hurowitz et al., 2023), but no 1.3–1.8 μm slope is visible in the IRS spectra of the Delta front, possible related to grain size effects. Units with strong near-IR signatures of sulfates also have a higher sulfur content, enough to be detected with LIBS (Wiens et al., 2022) and a higher CIA as well (> 50%, Dehouck et al. 2023). This supports deposition in an open system, *e.g.*, by evaporation of the Jezero lake (Mangold et al., 2021) or by fluvial/floodplain deposition (Broz et al. submitted). An abrasion patch was made in each of the three units: Uganik Island (Yori Pass), Berry Hollow (Hogwallow Flats), and Thornton Gap (lower Rockytop), and studied with all rover instruments. In all of these patches, Fe/Mg sulfates were detected by PIXL in the bulk (Hurowitz et al., 2023), as well as some occurrences of anhydrite veins (Jones et al., 2023). However, the Fe/Mg-carbonates suggested by the IRS and Triforce projection method alongside the sulfates are only supported by weak carbonate detections in Thornton Gap by PIXL (Hurowitz et al., 2023). The Devils Tanyard and Hughes River Gap units are different with strong signatures of Fe/Mg phyllosilicates and signatures suggesting the presence of vermiculite and smectite (Dehouck et al., 2023) with little or no carbonates. PIXL measurements also show the presence of phyllosilicates but also primary minerals (basaltic sediments) and a small amount of sulfates, not apparent in near-IR spectra (Hurowitz et al., 2023).

Higher above the delta front, the units of the Upper delta (Tenby formation) and the Margin unit are mainly characterized by a strong Fe^{2+} signature (1.3–1.8 μm slope) and bands at 1.93, 2.31, 2.39, and 2.51–2.53 μm associated with mixtures of Fe/Mg phyllosilicates (particularly smectites), carbonates, and a phase shifting the 1.9 μm band towards longer wavelengths like a Fe hydroxide or Fe/Mg sulfate. The position of the 2.3 μm band (Fe/Mg-OH and CO_3) varies little along the traverse with a majority of detections centered at 2.31 μm, corresponding to Fe and Mg-balanced phyllosilicates mixed with carbonates, but units at the entrance of the Margin unit (H. A. Memorial, Turquoise Bay) show some occurrences more enriched in Fe with a 2.29 μm band. The 2.5 μm band, on the other hand, exhibits more variability with a non-monotonic decrease in its position: from 2.53 μm (Fe-carbonates) in Carew Castle to < 2.52 μm (Fe/Mg-carbonates) in Bunsen Peak, with some occurrences particularly enriched in Mg (at 2.50 μm). This Mg content property is confirmed by Raman and LIBS analyses of SuperCam (Clavé et al., 2024), suggesting a Mg# between 30 and 70%. Proximity analyses performed by PIXL also show the presence of Fe/Mg-carbonates as clasts distributed throughout the rock as well as primary minerals (olivine, feldspar, augite) altered into phyllosilicates (Siebach et al., 2024). Unlike the Shenandoah formation, rocks from the Upper delta and the Margin unit exhibit a 2.21–2.22 μm band compatible with hydrated silica (Si-OH) presence. This mineral was also identified in PIXL measurements (Siebach et al., 2024; Beck et al., 2024a) as cement between clasts of primary minerals and carbonates. Finally, boulders have been identified in the Tenby formation, exhibiting near-IR spectra very different from those of the underlying bedrock. They are distributed into two types: those with a broad absorption band at 2 μm attributable to low calcium pyroxene (LCP) with little or no hydration signatures (Pyroxene-rich boulders) and those with a significant 1.3–1.8 μm slope and bands at 1.94 and 2.32 μm attributable to a mixture of olivine, serpentine, and Fe oxyhydroxide (olivine-rich boulders). Their oxide composition is consistent with these near-IR signatures, and corresponds to primitive igneous rocks: the olivine-rich are similar to Séítah as an ultramafic cumulate (Beyssac et al., 2024) albeit with a higher Mg content than Séítah, and the pyroxene-rich represent an even more primitive magma, possibly originating from Noachian terrains (Dehouck et al., 2024).

5. Conclusion

The Triforce projection compared to band position distribution analysis was demonstrated to be an effective tool for rapidly determining the main mineral components of rocks observed by the instrument IRS/Supercam onboard *Perseverance*. Projection onto ternary diagrams reveals compositional trends of mixtures where measurements cluster into distinct groups, while detailed examination of absorption band positions exposes the diversity of mineral species present. The uniqueness of this study lies in considering the entirety of the dataset as a coherent whole and comparing the occurrence and composition of

mineral assemblages throughout the rover traverse. It unveiled a significant diversity of primary mineral assemblages and alteration products, including Fe/Mg-smectites, Fe/Mg-carbonates, sulfates, hydrated silica, olivine, and pyroxene, partly consistent with previous IRS-based analyses and related investigations conducted by other instruments onboard the *Perseverance* rover.

This analysis provides a detailed overview for the nature, occurrence, and distribution of aqueous mineral-bearing deposits in Jezero crater. Although the orbital view that the deltaic deposits contain predominantly carbonates +/− phyllosilicates is confirmed, evidence now indicates that a far greater variety of alteration products occur at local scales in various geologic settings than was believed prior to *Perseverance*. These alteration products represent numerous distinct deposits having characteristic mineral assemblages that occur in bulk rocks, coatings, and soils with characteristic textural and lithological features in distinct geologic stratigraphy. These classes of deposits record periods of Jezero crater history during which liquid water persisted long enough to leave a mineral record, and they represent diverse aqueous environments with differing pH, cation chemistry and water activity levels. As such, they include a record of those deposits that possibly were habitable and sustained conditions necessary to preserve a fossil record of biotic or prebiotic evolution.

Future rover investigations supported by geochemical modeling and in depth cross-comparisons between different techniques ultimately are required to distinguish among competing hypotheses for their origins. Local variations of secondary phases record formative alteration events in the deltaic deposits and crater floor that could be related to the planet's early history and aid in the interpretation of past sedimentary processes and climate. It is therefore critical to determine if, and how, the modal composition of the deposits vary in space and time.

Open research

All reflectance-calibrated (calibration described in Royer et al. 2023) data supporting this study are accessible through the NASA Planetary Data System (Maurice et al., 2021) in FITS format, the list of used observations is provided in Supplementary Materials. A list of used laboratory spectra is also given in Supplementary Materials and come from RELAB (Milliken 2020, https://pds-speclib.rsl.wustl.edu/search.aspx?catalog=RELAB) and USGS (Kokaly et al., 2017).

CRediT authorship contribution statement

C. Royer: Writing – original draft, Methodology, Investigation, Data curation. **F. Poulet:** Writing – review & editing. **R.C. Wiens:** Writing – review & editing. **F. Montmessin:** Writing – review & editing. **P. Beck:** Writing – review & editing. **O. Beyssac:** Writing – review & editing. **É. Clavé:** Writing – review & editing, Conceptualization. **E. Dehouck:** Writing – review & editing. **T. Fouchet:** Writing – review & editing. **J.R. Johnson:** Writing – review & editing. **L. Mandon:** Writing – review & editing. **S. Bernard:** Writing – review & editing. **G. Caravaca:** Writing – review & editing. **S. le Mouélic:** Writing – review & editing. **C. Pilorget:** Writing – review & editing. **C. Quantin-Nataf:** Writing – review & editing. **S. Maurice:** Writing – review & editing. **A. Cousin:** Writing – review & editing.

Declaration of competing interest

The authors declare that they have no known competing financial interests or personal relationships that could have appeared to influence the work reported in this paper.

Acknowledgments

We thank all those who contributed to the development of the mission, especially the IRS, and to operating the Perseverance rover and SuperCam instrument to take the data. This work was supported in France by CNES and CNRS, and in the US by NASA's Mars Exploration Program, including NNH13ZDA018O.

Appendix A. Supplementary data

Supplementary material related to this article can be found online at https://doi.org/10.1016/j.icarus.2025.116538.

Data availability

All the data are available on the SuperCam Bundle on the PDS repository. See in the manuscript for a link to the repository.

References

Adams, J.B., Smith, M.O., Johnson, P.E., 1986. Spectral mixture modeling: A new analysis of rock and soil types at the viking lander 1 site. J. Geophys. Res.: Solid Earth 91 (B8), 8098–8112.

Beck, P., Beyssac, O., Schmitt, B., Royer, C., Mandon, L., Boulard, E., Rividi, N., Cloutis, E.A., 2024a. Quantification of crystal chemistry of Fe-Mg carbonates by Raman microspectroscopy and near-infrared remote sensing. Earth Space Sci. 11 (9), e2024EA003666.

Beck, P., Dehouck, E., Beyssac, O., Forni, O., Clavé, E., Bernard, S., Cloutis, E.A., Mandon, L., Royer, C., Rapin, W., Schroder, S., Francis, R., Mangold, N., Johnson, J.R., Quantin-Nataf, C., Poulet, F., Fouchet, T., Pilorget, C., Bedford, C.C., Gabriel, T.S.J., Madariaga, J.M., Clegg, S., Cousin, A., Wiens, R.C., Maurice, S., 2024b. SuperCam detections of hydrated-silica in the jezero crater. 3040, p. 1304.

Beyssac, O., Clavé, E., Udry, A., Dehouck, E., Forni, O., Quantin-Nataf, C., Lopez-Reyes, G., Beck, P., Royer, C., Gabriel, T., Kah, L.C., Schroeder, S., Johnson, J.R., Fouchet, T., Simon, J., Cousin, A., Maurice, S., Wiens, R.C., 2024. What are the olivine-rich boulders in the upper fan and margin unit at jezero crater, mars?. 3040, p. 1493.

Beyssac, O., Forni, O., Cousin, A., Udry, A., Kah, L., Mandon, L., Clavé, E., Liu, Y., Poulet, F., Quantin Nataf, C., Gasnault, O., Johnson, J., Benzerara, K., Beck, P., Dehouck, E., Mangold, N., Alvarez Llamas, C., Anderson, R., Arana, G., Barnes, R., Bernard, S., Bosak, T., Brown, A., Castro, K., Chide, B., Clegg, S., Cloutis, E., Fouchet, T., Gabriel, T., Gupta, S., Lacombe, G., Lasue, J., Le Mouelic, S., Lopez-Reyes, G., Madariaga, J., McCubbin, F., McLennan, S., Manrique, J., Meslin, P., Montmessin, F., Núñez, J., Ollila, A., Ostwald, A., Pilleri, P., Pinet, P., Royer, C., Sharma, S., Schröder, S., Simon, J., Toplis, M., Veneranda, M., Willis, P., Maurice, S., Wiens, R., Team, T.S., 2023. Petrological traverse of the olivine cumulate séítah formation at jezero crater, mars : A perspective from SuperCam onboard perseverance. J. Geophys. Res.: Planets n/a (128), e2022JE007638.

Bishop, J.L., King, S.J., Lane, M.D., Brown, A.J., Lafuente, B., Hiroi, T., Roberts, R., Swayze, G.A., Lin, J.-F., Sánchez Román, M., 2021. Spectral properties of anhydrous carbonates and nitrates. Earth Space Sci. 8 (10), e2021EA001844.

Bishop, J.L., Lane, M.D., Dyar, M.D., Brown, A.J., 2008. Reflectance and emission spectroscopy study of four groups of phyllosilicates: Smectites, kaolinite-serpentines, chlorites and micas. Clay Miner. 43 (1), 35–54.

Brown, A.J., 2006. Spectral curve fitting for automatic hyperspectral data analysis. IEEE Trans. Geosci. Remote Sens. 44, 1601–1608.

Brown, A.J., Viviano, C.E., Goudge, T.A., 2020. Olivine-carbonate mineralogy of the Jezero Crater Region. J. Geophys. Res.: Planets 125 (3), e2019JE006011.

Burns, R.G., 1970. Crystal field spectra and evidence of cation ordering in olivine Minerals1. Am. Mineral. 55 (9–10), 1608–1632.

Burns, R.G., 1993. Mineralogical Applications of Crystal Field Theory. Cambridge University Press.

Califano, S., Schettino, V., Neto, N., 1981. Lattice dynamics of molecular crystals. In: Berthier, G., Dewar, M.J.S., Fischer, H., Fukui, K., Hall, G.G., Hartmann, H., Jaffé, H.H., Jortner, J., Kutzelnigg, W., Ruedenberg, K., Scrocco, E. (Eds.), In: Lecture Notes in Chemistry, vol. 26, Springer, Berlin, Heidelberg.

Carter, J., Poulet, F., Bibring, J.-P., Mangold, N., Murchie, S., 2013. Hydrous minerals on mars as seen by the CRISM and OMEGA imaging spectrometers: updated global view. J. Geophys. Res.: Planets 118 (4), 831–858.

Carter, J., Riu, L., Poulet, F., Bibring, J.-P., Langevin, Y., Gondet, B., 2023. A mars orbital catalog of aqueous alteration signatures (MOCAAS). Icarus 389, 115164.

Clark, R.N., King, T.V.V., 1987. Automatic continuum analysis of reflectance spectra.

Clark, R.N., King, T.V.V., Klejwa, M., Swayze, G.A., Vergo, N., 1990. High spectral resolution reflectance spectroscopy of minerals. J. Geophys. Res.: Solid Earth 95 (B8), 12653–12680.

Clark, R.N., Swayze, G.A., Livo, K.E., Kokaly, R.F., Sutley, S.J., Dalton, J.B., McDougal, R.R., Gent, C.A., 2003. Imaging spectroscopy: earth and planetary remote sensing with the USGS tetracorder and expert systems: imaging spectroscopy remote sensing. J. Geophys. Res.: Planets 108 (12).

Clavé, E., Beck, P., Dehouck, E., Forni, O., Schröder, S., Mangold, N., Royer, C., Mandon, L., Le Mouélic, S., Quantin-Nataf, C., Bernard, S., Madariaga, J.A., Lopez-Reyes, G., Ollila, A., Johnson, J., Clegg, S., Cousin, A., Wiens, R.C., Maurice, S., 2024. Diversity of carbonates in jezero crater, mars, as seen with the SuperCam instrument. 3040, p. 1829.

Clavé, E., Benzerara, K., Meslin, P.-Y., Forni, O., Royer, C., Mandon, L., Beck, P., Quantin-Nataf, C., Beyssac, O., Cousin, A., Bousquet, B., Wiens, R.C., Maurice, S., Dehouck, E., Schröder, S., Gasnault, O., Mangold, N., Dromart, G., Bosak, T., Bernard, S., Udry, A., Anderson, R.B., Arana, G., Brown, A.J., Castro, K., Clegg, S.M., Cloutis, E., Fairén, A.G., Flannery, D.T., Gasda, P.J., Johnson, J.R., Lasue, J., Lopez-Reyes, G., Madariaga, J.M., Manrique, J.A., Le Mouélic, S., Núñez, J.I., Ollila, A.M., Pilleri, P., Pilorget, C., Pinet, P., Poulet, F., Veneranda, M., Wolf, Z.U., Team, t.S., 2023. Carbonate detection with SuperCam in igneous rocks on the floor of jezero crater, mars. J. Geophys. Res.: Planets 128 (6), e2022JE007463.

Clenet, H., Pinet, P., Ceuleneer, G., Daydou, Y., Heuripeau, F., Rosemberg, C., Bibring, J.-P., Bellucci, G., Altieri, F., Gondet, B., 2013. A systematic mapping procedure based on the modified Gaussian model to characterize magmatic units from olivine/pyroxenes mixtures: application to the syrtis major volcanic shield on mars. J. Geophys. Res.: Planets 118 (8), 1632–1655.

Cloutis, E.A., Asher, P.M., Mertzman, S.A., 2002. Spectral reflectance properties of zeolites and remote sensing implications. J. Geophys. Res.: Planets 107 (E9), 5–1–5–19.

Cloutis, E.A., Craig, M.A., Kruzelecky, R.V., Jamroz, W.R., Scott, A., Hawthorne, F.C., Mertzman, S.A., 2008. Spectral reflectance properties of minerals exposed to simulated mars surface conditions. Icarus 195 (1), 140–168.

Cloutis, E.A., Craig, M.A., Mustard, J.F., Kruzelecky, R.V., Jamroz, W.R., Scott, A., Bish, D.L., Poulet, F., Bibring, J.-P., King, P.L., 2007. Stability of hydrated minerals on mars. Geophys. Res. Lett. 34 (20).

Combe, J.P., Le Mouélic, S., Sotin, C., Gendrin, A., Mustard, J.F., Le Deit, L., Launeau, P., Bibring, J.P., Gondet, B., Langevin, Y., Pinet, P., 2008. Analysis of OMEGA/Mars Express data hyperspectral data using a multiple-endmember linear spectral unmixing model (MELSUM): methodology and first results. Planet. Space Sci. 56 (7), 951–975.

Corpolongo, A., Jakubek, R.S., Burton, A.S., Brown, A.J., Yanchilina, A., Czaja, A.D., Steele, A., Wogsland, B.V., Lee, C., Flannery, D., Baker, D., Cloutis, E.A., Cardarelli, E., Scheller, E.L., Berger, E.L., McCubbin, F.M., Hollis, J.R., Hickman-Lewis, K., Steadman, K., Uckert, K., DeFlores, L., Kah, L., Beegle, L.W., Fries, M., Minitti, M., Haney, N.C., Conrad, P., Morris, R.V., Bhartia, R., Roppel, R., Siljeström, S., Asher, S.A., Bykov, S.V., Sharma, S., Shkolyar, S., Fornaro, T., Abbey, W., 2023. SHERLOC Raman mineral class detections of the mars 2020 crater floor campaign. J. Geophys. Res.: Planets 128 (3), e2022JE007455.

Dalton, J.B., 2003. Spectral behavior of hydrated sulfate salts: implications for europa mission spectrometer design. Astrobiology 3 (4), 771–784.

Dehouck, E., Clavé, E., Beyssac, O., Quantin-Nataf, C., Udry, A., Forni, O., Mangold, N., Beck, P., Johnson, J.R., Schröder, S., Simon, J.I., Fouchet, T., Cousin, A., Maurice, S., Wiens, R.C., 2024. Pristine pyroxene-bearing boulders analyzed by SuperCam in the jezero western fan, mars. 3040, p. 1967.

Dehouck, E., Forni, O., Quantin-Nataf, C., Beck, P., Mangold, N., Royer, C., Clavé, E., Beyssac, O., Johnson, J.R., Mandon, L., Poulet, F., Le Mouélic, S., Caravaca, G., Kalucha, H., Gibbons, E., Dromart, G., Gasda, P., Meslin, P.Y., Schroeder, S., Udry, A., Anderson, R.B., Clegg, S., Cousin, A., Gabriel, T.S., Lasue, J., Fouchet, T., Pilleri, P., Pilorget, C., Hurowitz, J., Núñez, J., Williams, A., Russell, P., Simon, J.I., Maurice, S., Wiens, R.C., SuperCam Team, 2023. Overview of the bedrock geochemistry and mineralogy observed by SuperCam during perseverance's delta front campaign. Lunar Planet. Sci. Contrib. 2806, 2862.

Ehlmann, B.L., Mustard, J.F., Swayze, G.A., Clark, R.N., Bishop, J.L., Poulet, F., Des Marais, D.J., Roach, L.H., Milliken, R.E., Wray, J.J., Barnouin-Jha, O., Murchie, S.L., 2009. Identification of hydrated silicate minerals on mars using MRO-CRISM: geologic context near nili fossae and implications for aqueous alteration. J. Geophys. Res. (Planets) 114, E00D08.

Farley, K.A., Stack, K.M., Shuster, D.L., Horgan, B.H.N., Hurowitz, J.A., Tarnas, J.D., Simon, J.I., Sun, V.Z., Scheller, E.L., Moore, K.R., McLennan, S.M., Vasconcelos, P.M., Wiens, R.C., Treiman, A.H., Mayhew, L.E., Beyssac, O., Kizovski, T.V., Tosca, N.J., Williford, K.H., Crumpler, L.S., Beegle, L.W., Bell, J.F., Ehlmann, B.L., Liu, Y., Maki, J.N., Schmidt, M.E., Allwood, A.C., Amundsen, H.E.F., Bhartia, R., Bosak, T., Brown, A.J., Clark, B.C., Cousin, A., Forni, O., Gabriel, T.S.J., Goreva, Y., Gupta, S., Hamran, S.-E., Herd, C.D.K., Hickman-Lewis, K., Johnson, J.R., Kah, L.C., Kelemen, P.B., Kinch, K.B., Mandon, L., Mangold, N., Quantin-Nataf, C., Rice, M.S., Russell, P.S., Sharma, S., Siljeström, S., Steele, A., Sullivan, R., Wadhwa, M., Weiss, B.P., Williams, A.J., Wogsland, B.V., Willis, P.A., Acosta-Maeda, T.A., Beck, P., Benzerara, K., Bernard, S., Burton, A.S., Cardarelli, E.L., Chide, B., Clavé, E., Cloutis, E.A., Cohen, B.A., Czaja, A.D., Debaille, V., Dehouck, E., Fairén, A.G., Flannery, D.T., Fleron, S.Z., Fouchet, T., Frydenvang, J., Garczynski, B.J., Gibbons, E.F., Hausrath, E.M., Hayes, A.G., Henneke, J., Jørgensen, J.L., Kelly, E.M., Lasue, J., Le Mouélic, S., Madariaga, J.M., Maurice, S., Merusi, M., Meslin, P.-Y., Milkovich, S.M., Million, C.C., Moeller, R.C., Núñez, J.I., Ollila, A.M., Paar, G., Paige, D.A., Pedersen, D.A.K., Pilleri, P., Pilorget, C., Pinet, P.C., Rice, J.W., Royer, C., Sautter, V., Schulte, M., Sephton, M.A., Sharma, S.K., Sholes, S.F., Spanovich, N., St. Clair, M., Tate, C.D., Uckert, K., VanBommel, S.J., Yanchilina, A.G., Zorzano, M.-P., 2022. Aqueously altered igneous rocks sampled on the floor of jezero crater, mars. Science 377 (6614), eabo2196.

Farley, K.A., Williford, K.H., Stack, K.M., Bhartia, R., Chen, A., de la Torre, M., Hand, K., Goreva, Y., Herd, C.D.K., Hueso, R., Liu, Y., Maki, J.N., Martinez, G., Moeller, R.C., Nelessen, A., Newman, C.E., Nunes, D., Ponce, A., Spanovich, N., Willis, P.A., Beegle, L.W., Bell, J.F., Brown, A.J., Hamran, S.-E., Hurowitz, J.A., Maurice, S., Paige, D.A., Rodriguez-Manfredi, J.A., Schulte, M., Wiens, R.C., 2020. Mars 2020 mission overview. Space Sci. Rev. 216 (8), 142.

Fassett, C.I., Head, III, J.W., 2005. Fluvial sedimentary deposits on mars: ancient deltas in a crater lake in the nili fossae region. Geophys. Res. Lett. 32 (14).

Fouchet, T., Reess, J.-M., Montmessin, F., Hassen-Khodja, R., Nguyen-Tuong, N., Humeau, O., Jacquinod, S., Lapauw, L., Parisot, J., Bonafous, M., Bernardi, P., Chapron, F., Jeanneau, A., Collin, C., Zeganadin, D., Nibert, P., Abbaki, S., Montaron, C., Blanchard, C., Arslanyan, V., Achelhi, O., Colon, C., Royer, C., Hamm, V., Beuzit, M., Poulet, F., Pilorget, C., Mandon, L., Forni, O., Cousin, A., Gasnault, O., Pilleri, P., Dubois, B., Quantin, C., Beck, P., Beyssac, O., Le Mouélic, S., Johnsson, J.R., McConnochie, T.H., Maurice, S., Wiens, R.C., 2022. The SuperCam infrared spectrometer for the perseverance rover of the mars2020 mission. Icarus 373, 114773.

Gaffey, S.J., 1987. Spectral reflectance of carbonate minerals in the visible and near infrared (0.35–2.55 um): anhydrous carbonate minerals. J. Geophys. Res.: Solid Earth 92 (B2), 1429–1440.

Goudge, T.A., Aureli, K.L., Head, J.W., Fassett, C.I., Mustard, J.F., 2015a. Classification and analysis of candidate impact crater-hosted closed-basin lakes on mars. Icarus 260, 346–367.

Goudge, T.A., Mustard, J.F., Head, J.W., Fassett, C.I., Wiseman, S.M., 2015b. Assessing the mineralogy of the watershed and fan deposits of the jezero crater paleolake system, mars. J. Geophys. Res.: Planets 120 (4), 775–808.

Gwizd, S., Stack, K.M., Ives, L., Gupta, S., Randazzo, N., Lamb, M., Cavallo, N., Williams, N., Crumpler, L., Rice, J., Horgan, B., Kah, L.C., Cianciolo, O., Quentin-Nataf, C., Beyssac, O., Vaughan, A., Simon, J.I., Siebach, K., Nachon, M., Kronyak, R., Sun, V., Sholes, S., Shuster, D., Bell, J., 2024. Depositional history of the upper sequence of the western fan: evidence for late-stage fluvial and potential igneous activity, jezero crater, mars. 3040, p. 2117.

Hapke, B., 1981. Bidirectional reflectance spectroscopy: 1. theory. J. Geophys. Res.: Solid Earth 86 (B4), 3039–3054.

Hapke, B., 1993. Theory of Reflectance and Emittance Spectroscopy. Cambridge University Press.

Horgan, B.H.N., Anderson, R.B., Dromart, G., Amador, E.S., Rice, M.S., 2020. The mineral diversity of jezero crater: evidence for possible lacustrine carbonates on mars. Icarus 339, 113526.

Hunt, G.R., Salisbury, J.W., 1970. Visible and near-infrared spectra of minerals and rocks: I silicate minerals. 1, pp. 283–300.

Hurowitz, J.A., Tice, M.M., Allwood, A.C., Cable, M.L., Bosak, T., Broz, A., Caravaca, G., Clark, B.C., Dehouck, E., Fairen, A., Gomez, F., Grotzinger, J.P., Gupta, S., Johnson, J.R., Kah, L.C., Kalucha, H., Labrie, J., Li, A.Y., Mandon, L., Nuñez, J., Pedersen, D.A.K., Poulet, F., Randazzo, N., Scheller, E.L., Schmidt, M.E., Shuster, D.L., Siebach, K.L., Siljeström, S., Simon, J.I., Tosca, N.J., Treiman, A.H., VanBommel, S.J., Wade, L.A., Williford, K.H., Yanchilina, A., 2023. The petrogenetic history of the jezero Crater Delta front from microscale observations by the mars 2020 PIXL instrument. 2806, p. 2301.

Isaacson, P.J., Pieters, C.M., Besse, S., Clark, R.N., Head, J.W., Klima, R.L., Mustard, J.F., Petro, N.E., Staid, M.I., Sunshine, J.M., Taylor, L.A., Thaisen, K.G., Tompkins, S., 2011. Remote compositional analysis of lunar olivine-rich lithologies with moon mineralogy mapper (M3) spectra. J. Geophys. Res.: Planets 116 (E6).

Ives, L.R.W., Stack, K.M., Barnes, R., Gupta, S., Caravaca, G., Russell, P., Annex, A.M., 2023. Lithofacies, flow directions, and preliminary depositional interpretations of ledge-forming sandstones at alagnak, jezero crater, mars. 2806, p. 2556.

Johnson, J.R., Bell, III, J.F., Cloutis, E., Staid, M., Farrand, W.H., McCoy, T., Rice, M., Wang, A., Yen, A., 2007. Mineralogic constraints on sulfur-rich soils from pancam spectra at gusev crater, mars. Geophys. Res. Lett. 34 (13).

Jones, M.W.M., Flannery, D.A., Orenstein, B.J., Hurowitz, J.A., Catling, D.C., Tice, M.M., Allwood, A.C., Heirwegh, C., Clark, B.C., VanBommel, S.J., Knight, A.L., 2023. Crystallography on mars: identification of crystalline anhydrite as a secondary mineral filling cavities and veinlets in the western Jezero Delta front. 2806, p. 3006.

Kanner, L.C., Mustard, J.F., Gendrin, A., 2007. Assessing the limits of the modified Gaussian model for remote spectroscopic studies of pyroxenes on mars. Icarus 187 (2), 442–456.

Kokaly, R., Clark, R.N., Swayze, G.A., Livo, K.E., Hoefen, T.M., Pearson, N.C., Wise, R.A., Benzel, W.M., Lowers, H.A., Driscoll, R.L., Klein, A.J., 2017. USGS Spectral Library Version 7 Data. U.S. Geological Survey.

Le Mouelic, S., Combe, J.-P., Sarago, V., Mangold, N., Masse, M., Bibring, J.-P., Gondet, B., Langevin, Y., Sotin, C., 2009. An iterative least squares approach to decorrelate minerals and ices contributions in hyperspectral images: application to cuprite (earth) and mars. In: 2009 First Workshop on Hyperspectral Image and Signal Processing: Evolution in Remote Sensing. pp. 1–4.

Liu, Y., Tice, M.M., Schmidt, M.E., Treiman, A.H., Kizovski, T.V., Hurowitz, J.A., Allwood, A.C., Henneke, J., Pedersen, D.A.K., VanBommel, S.J., Jones, M.W.M., Knight, A.L., Orenstein, B.J., Clark, B.C., Elam, W.T., Heirwegh, C.M., Barber, T., Beegle, L.W., Benzerara, K., Bernard, S., Beyssac, O., Bosak, T., Brown, A.J., Cardarelli, E.L., Catling, D.C., Christian, J.R., Cloutis, E.A., Cohen, B.A., Davidoff, S., Fairén, A.G., Farley, K.A., Flannery, D.T., Galvin, A., Grotzinger, J.P.,

Gupta, S., Hall, J., Herd, C.D.K., Hickman-Lewis, K., Hodyss, R.P., Horgan, B.H.N., Johnson, J.R., Jørgensen, J.L., Kah, L.C., Maki, J.N., Mandon, L., Mangold, N., McCubbin, F.M., McLennan, S.M., Moore, K., Nachon, M., Nemere, P., Nothdurft, L.D., Núñez, J.I., O'Neil, L., Quantin-Nataf, C.M., Sautter, V., Shuster, D.L., Siebach, K.L., Simon, J.I., Sinclair, K.P., Stack, K.M., Steele, A., Tarnas, J.D., Tosca, N.J., Uckert, K., Udry, A., Wade, L.A., Weiss, B.P., Wiens, R.C., Williford, K.H., Zorzano, M.-P., 2022. An olivine cumulate outcrop on the floor of jezero crater, mars. Science 377 (6614), 1513–1519.

Maki, J.N., Farley, K., Stack, K., Calef, F., Williams, N., Bell, III, J.F., Herd, C.D.K., Wadhwa, M., Brown, A., 2023. The mars 2020 three forks sample depot. 2806, p. 2875.

Mandon, L., Quantin-Nataf, C., Royer, C., Beck, P., Fouchet, T., Johnson, J.R., Dehouck, E., Le Mouélic, S., Poulet, F., Montmessin, F., Pilorget, C., Gasnault, O., Forni, O., Mayhew, L.E., Beyssac, O., Bertrand, T., Clavé, E., Pinet, P., Brown, A.J., Legett, C., Tarnas, J., Cloutis, E.A., Poggiali, G., Fornaro, T., Maurice, S., Wiens, R.C., Team, T.S., 2023. Reflectance of jezero crater floor: 2. mineralogical interpretation. J. Geophys. Res.: Planets 128 (7), e2022JE007450.

Mangold, N., Dromart, G., Ansan, V., Salese, F., Kleinhans, M.G., Massé, M., Quantin-Nataf, C., Stack, K.M., 2020. Fluvial regimes, morphometry, and age of jezero crater paleolake inlet valleys and their exobiological significance for the 2020 rover mission landing site. Astrobiology 20 (8), 994–1013.

Mangold, N., Gupta, S., Gasnault, O., Dromart, G., Tarnas, J.D., Sholes, S.F., Horgan, B., Quantin-Nataf, C., Brown, A.J., Mouélic, S.L., Yingst, R.A., Bell, J.F., Beyssac, O., Bosak, T., CalefIII, F., Ehlmann, B.L., Farley, K.A., Grotzinger, J.P., Hickman-Lewis, K., Holm-Alwmark, S., Kah, L.C., Martinez-Frias, J., McLennan, S.M., Maurice, S., Nuñez, J.I., Ollila, A.M., Pilleri, P., RiceJr, J.W., Rice, M., Simon, J.I., Shuster, D.L., Stack, K.M., Sun, V.Z., Treiman, A.H., Weiss, B.P., Wiens, R.C., Williams, A.J., Williams, N.R., Williford, K.H., 2021. Perseverance rover reveals an Ancient Delta-lake system and flood deposits at jezero crater, mars. Science 374 (6568), 711–717.

Manrique, J.A., Lopez-Reyes, G., Cousin, A., Rull, F., Maurice, S., Wiens, R.C., Madsen, M.B., Madariaga, J.M., Gasnault, O., Aramendia, J., Arana, G., Beck, P., Bernard, S., Bernardi, P., Bernt, M.H., Berrocal, A., Beyssac, O., Caïs, P., Castro, C., Castro, K., Clegg, S.M., Cloutis, E., Dromart, G., Drouet, C., Dubois, B., Escribano, D., Fabre, C., Fernandez, A., Forni, O., Garcia-Baonza, V., Gontijo, I., Johnson, J., Laserna, J., Lasue, J., Madsen, S., Mateo-Marti, E., Medina, J., Meslin, P.-Y., Montagnac, G., Moral, A., Moros, J., Ollila, A.M., Ortega, C., Prieto-Ballesteros, O., Reess, J.M., Robinson, S., Rodriguez, J., Saiz, J., Sanz-Arranz, J.A., Sard, I., Sautter, V., Sobron, P., Toplis, M., Veneranda, M., 2020. SuperCam calibration targets: design and development. Space Sci. Rev. 216 (8), 138.

Maurice, S.A., Wiens, R.C., 2021. Mars 2020 SuperCam bundle. http://dx.doi.org/10.17189/1522646.

Maurice, S., Wiens, R.C., Bernardi, P., Caïs, P., Robinson, S., Nelson, T., Gasnault, O., Reess, J.-M., Deleuze, M., Rull, F., Manrique, J.-A., Abbaki, S., Anderson, R.B., André, Y., Angel, S.M., Arana, G., Battault, T., Beck, P., Benzerara, K., Bernard, S., Berthias, J.-P., Beyssac, O., Bonafous, M., Bousquet, B., Boutillier, M., Cadu, A., Castro, K., Chapron, F., Chide, B., Clark, K., Clavé, E., Clegg, S., Cloutis, E., Collin, C., Cordoba, E.C., Cousin, A., Dameury, J.-C., D'Anna, W., Daydou, Y., Debus, A., Deflores, L., Dehouck, E., Delapp, D., De Los Santos, G., Donny, C., Doressoundiram, A., Dromart, G., Dubois, B., Dufour, A., Dupieux, M., Egan, M., Ervin, J., Fabre, C., Fau, A., Fischer, W., Forni, O., Fouchet, T., Frydenvang, J., Gauffre, S., Gauthier, M., Gharakanian, V., Gilard, O., Gontijo, I., Gonzalez, R., Granena, D., Grotzinger, J., Hassen-Khodja, R., Heim, M., Hello, Y., Hervet, G., Humeau, O., Jacob, X., Jacquinod, S., Johnson, J.R., Kouach, D., Lacombe, G., Lanza, N., Lapauw, L., Laserna, J., Lasue, J., Le Deit, L., Le Mouélic, S., Le Comte, E., Lee, Q.-M., Legett, C., Leveille, R., Lewin, E., Leyrat, C., Lopez-Reyes, G., Lorenz, R., Lucero, B., Madariaga, J.M., Madsen, S., Madsen, M., Mangold, N., Manni, F., Mariscal, J.-F., Martinez-Frias, J., Mathieu, K., Mathon, R., McCabe, K.P., McConnochie, T., McLennan, S.M., Mekki, J., Melikechi, N., Meslin, P.-Y., Micheau, Y., Michel, Y., Michel, J.M., Mimoun, D., Misra, A., Montagnac, G., Montaron, C., Montmessin, F., Moros, J., Mousset, V., Morizet, Y., Murdoch, N., Newell, R.T., Newsom, H., Nguyen Tuong, N., Ollila, A.M., Orttner, G., Oudda, L., Pares, L., Parisot, J., Parot, Y., Pérez, R., Pheav, D., Picot, L., Pilleri, P., Pilorget, C., Pinet, P., Pont, G., Poulet, F., Quantin-Nataf, C., Quertier, B., Rambaud, D., Rapin, W., Romano, P., Roucayrol, L., Royer, C., Ruellan, M., Sandoval, B.F., Sautter, V., Schoppers, M.J., Schröder, S., Seran, H.-C., Sharma, S.K., Sobron, P., Sodki, M., Sournac, A., Sridhar, V., Standarovsky, D., Storms, S., Striebig, N., Tatat, M., Toplis, M., Torre-Fdez, I., Toulemont, N., Velasco, C., Veneranda, M., Venhaus, D., Virmontois, C., Viso, M., Willis, P., Wong, K.W., 2021. The SuperCam instrument suite on the mars 2020 rover: science objectives and mast-unit description. Space Sci. Rev. 217 (3), 47.

Merényi, E., Singer, R.B., Miller, J.S., 1996. Mapping of spectral variations on the surface of mars from high spectral resolution telescopic images. Icarus 124 (1), 280–295.

Milliken, R., 2020. RELAB spectral library bundle. http://dx.doi.org/10.17189/1519032.

Moreland, E.L., Siebach, K.L., Liu, Y., Treiman, A.H., Tice, M.M., Hurowitz, J.A., Gasada, P.J., Kizovski, T.V., Clark, B.C., Costin, G., Allwood, A., 2024. Falcon lake: An olivine-rich boulder in jezero crater, mars. 3040, p. 2030.

Murchie, S., Arvidson, R., Bedini, P., Beisser, K., Bibring, J.-P., Bishop, J., Boldt, J., Cavender, P., Choo, T., Clancy, R.T., Darlington, E.H., Des Marais, D., Espiritu, R., Fort, D., Green, R., Guinness, E., Hayes, J., Hash, C., Heffernan, K., Hemmler, J., Heyler, G., Humm, D., Hutcheson, J., Izenberg, N., Lee, R., Lees, J., Lohr, D., Malaret, E., Martin, T., McGovern, J.A., McGuire, P., Morris, R., Mustard, J., Pelkey, S., Rhodes, E., Robinson, M., Roush, T., Schaefer, E., Seagrave, G., Seelos, F., Silverglate, P., Slavney, S., Smith, M., Shyong, W.-J., Strohbehn, K., Taylor, H., Thompson, P., Tossman, B., Wirzburger, M., Wolff, M., 2007. Compact reconnaissance imaging spectrometer for mars (CRISM) on mars reconnaissance orbiter (MRO). J. Geophys. Res. (Planets) 112 (E5), E05S03.

Paige, D.A., Hamran, S.-E., Amundsen, H.E.F., Berger, T., Berman, D.A., Brovoll, S., Carter, L.M., Casademont, T., Damsgard, L., Dypvik, H., Eide, S., Ghent, R.R., Kakaria, R., Kohler, J., Mellon, M.T., Nunes, D.C., Plettemeier, D., Russell, P., Shoemaker, E., Siegler, M., 2022. Mars perseverance RIMFAX ground penetrating radar stratigraphy of the jezero Crater Delta / crater floor contact. 2022, pp. P55A–05.

Parente, M., Makarewicz, H.D., Bishop, J.L., 2011. Decomposition of mineral absorption bands using nonlinear least squares curve fitting: application to martian meteorites and CRISM data. Planet. Space Sci. 59 (5), 423–442.

Pinet, P.C., Daydou, Y.H., Chevrel, S.D., 2022. Olivine composition and reflectance spectroscopy relationship revisited from advanced MGM deconvolution based on synthetic and natural samples. Icarus 373, 114765.

Poitras, J.T., Cloutis, E.A., Salvatore, M.R., Mertzman, S.A., Applin, D.M., Mann, P., 2018. Mars analog minerals' spectral reflectance characteristics under martian surface conditions. Icarus 306, 50–73.

Royer, C., Fouchet, T., Mandon, L., Montmessin, F., Poulet, F., Forni, O., Johnson, J.R., Legett, C., Le Mouélic, S., Gasnault, O., Quantin-Nataf, C., Beck, P., Dehouck, E., Clavé, E., Ollila, A.M., Pilorget, C., Bernardi, P., Reess, J.-M., Pilleri, P., Brown, A., Newell, R.T., Cloutis, E., Maurice, S., Wiens, R.C., Team, T.S., 2023. Reflectance of jezero crater floor: 1. data processing and calibration of the infrared spectrometer (IRS) on SuperCam. J. Geophys. Res.: Planets 128 (1).

Savitzky, A., Golay, M.J.E., 1964. Smoothing and differentiation of data by simplified least squares procedures. Anal. Chem. 36 (8), 1627–1639.

Schon, S.C., Head, J.W., Fassett, C.I., 2012. An overfilled lacustrine system and Progradational Delta in jezero crater, mars: implications for noachian climate. Planet. Space Sci. 67 (1), 28–45.

Sheppard, R., Loizeau, D., Rampe, E.B., Fraeman, A.A., 2024. The presence of Mg sulfate can obscure spectral evidence of siderite. LPI Contrib. 55 (2008).

Shkuratov, Y., Starukhina, L., Hoffmann, H., Arnold, G., 1999. A model of spectral albedo of particulate surfaces: implications for optical properties of the moon. Icarus 137 (2), 235–246.

Siebach, K.L., Tice, M.M., Hurowitz, J.A., Moreland, E.L., Van Beek, J.K., Kizovski, T.V., Schmidt, M., O'Neil, L.P., Treiman, A.H., Allwood, A.C., Cable, M.L., Nachon, M., Gupta, S., 2024. PIXL analyses of sedimentary rocks in the mars 2020 perseverance upper fan campaign in jezero crater. 3040, p. 2365.

Siljeström, S., Czaja, A.D., Corpolongo, A., Berger, E.L., Li, A.Y., Cardarelli, E., Abbey, W., Asher, S.A., Beegle, L.W., Benison, K.C., Bhartia, R., Bleefeld, B.L., Burton, A.S., Bykov, S.V., Clark, B., DeFlores, L., Ehlmann, B.L., Fornaro, T., Fox, A., Gómez, F., Hand, K., Haney, N.C., Hickman-Lewis, K., Hug, W.F., Imbeah, S., Jakubek, R.S., Kah, L.C., Kivrak, L., Lee, C., Liu, Y., Martínez-Frías, J., McCubbin, F.M., Minitti, M., Moore, K., Morris, R.V., Núñez, J.I., Osterhout, J.T., Phua, Y.Y., Randazzo, N., Hollis, J.R., Rodriguez, C., Roppel, R., Scheller, E.L., Sephton, M., Sharma, S.K., Sharma, S., Steadman, K., Steele, A., Tice, M., Uckert, K., VanBommel, S., Williams, A.J., Williford, K.H., Winchell, K., Wu, M.K., Yanchilina, A., Zorzano, M.-P., 2024. Evidence of sulfate-rich fluid alteration in jezero crater floor, mars. J. Geophys. Res.: Planets 129 (1), e2023JE007989.

Stack, K.M., Ives, L.R.W., Gupta, S., Lamb, M.P., Tebolt, M., Caravaca, G., Grotzinger, J.P., Russell, P., Shuster, D.L., Williams, A.J., Amundsen, H., Alwmark, S., Annex, A.M., Barnes, R., Bell, III, J., Beyssac, O., Bosak, T., Crumpler, L.S., Dehouck, E., Gwizd, S.J., Hickman-Lewis, K., Horgan, B.H.N., Hurowitz, J., Kalucha, H., Kanine, O., Lesh, C., Maki, J., Mangold, N., Randazzo, N., Seeger, C., Williams, R.M.E., Brown, A., Cardarelli, E., Dypvik, H., Flannery, D., Frydenvang, J., Hamran, S.-E., Núñez, J.I., Paige, D., Simon, J.I., Tice, M., Tate, C., Wiens, R.C., 2024. Sedimentology and stratigraphy of the shenandoah formation, western fan, jezero crater, mars. J. Geophys. Res.: Planets 129 (2), e2023JE008187.

Steinier, J., Termonia, Y., Deltour, J., 1972. Comments on smoothing and differentiation of data by simplified least square procedure. Anal. Chem. 44 (11), 1906–1909.

Sunshine, J.M., Pieters, C.M., Pratt, S.F., 1990. Deconvolution of mineral absorption bands: An improved approach. J. Geophys. Res.: Solid Earth 95 (B5), 6955–6966.

Swayze, G.A., Lowers, H.A., Benzel, W.M., Clark, R.N., Driscoll, R.L., Perlman, Z.S., Hoefen, T.M., Dyar, M.D., 2018. Characterizing the source of potentially asbestos-bearing commercial vermiculite insulation using in situ IR spectroscopy. Am. Mineral. 103 (4), 517–549.

Tarnas, J.D., Mustard, J.F., Lin, H., Goudge, T.A., Amador, E.S., Bramble, M.S., Kremer, C.H., Zhang, X., Itoh, Y., Parente, M., 2019. Orbital identification of hydrated silica in jezero crater, mars. Geophys. Res. Lett. 46 (22), 12771–12782.

Tarnas, J.D., Stack, K.M., Parente, M., Koeppel, A.H.D., Mustard, J.F., Moore, K.R., Horgan, B.H.N., Seelos, F.P., Cloutis, E.A., Kelemen, P.B., Flannery, D., Brown, A.J., Frizzell, K.R., Pinet, P., 2021. Characteristics, origins, and biosignature preservation potential of carbonate-bearing rocks within and outside of jezero crater. J. Geophys. Res.: Planets 126 (11), e2021JE006898.

Tice, M.M., Hurowitz, J.A., Allwood, A.C., Jones, M.W.M., Orenstein, B.J., Davidoff, S., Wright, A.P., Pedersen, D.A., Henneke, J., Tosca, N.J., Moore, K.R., Clark, B.C., McLennan, S.M., Flannery, D.T., Steele, A., Brown, A.J., Zorzano, M.-P., Hickman-Lewis, K., Liu, Y., VanBommel, S.J., Schmidt, M.E., Kizovski, T.V., Treiman, A.H., O'Neil, L., Fairén, A.G., Shuster, D.L., Gupta, S., THE PIXL TEAM, 2022. Alteration history of séítah formation rocks inferred by PIXL X-Ray fluorescence, x-ray diffraction, and multispectral imaging on mars. Sci. Adv. 8 (47), eabp9084.

Udry, A., Ostwald, A., Sautter, V., Cousin, A., Beyssac, O., Forni, O., Dromart, G., Benzerara, K., Nachon, M., Horgan, B., Mandon, L., Clavé, E., Dehouck, E., Gibbons, E., Alwmark, S., Ravanis, E., Wiens, R.C., Legett, C., Anderson, R., Pilleri, P., Mangold, N., Schmidt, M., Liu, Y., Núñez, J.I., Castro, K., Madariaga, J.M., Kizovski, T., Beck, P., Bernard, S., Bosak, T., Brown, A., Clegg, S., Cloutis, E., Cohen, B., Connell, S., Crumpler, L., Debaille, V., Flannery, D., Fouchet, T., Gabriel, T.S.J., Gasnault, O., Herd, C.D.K., Johnson, J., Manrique, J.A., Maurice, S., McCubbin, F.M., McLennan, S., Ollila, A., Pinet, P., Quantin-Nataf, C., Royer, C., Sharma, S., Simon, J.I., Steele, A., Tosca, N., Treiman, A., Team, t.S., 2023. A mars 2020 perseverance SuperCam perspective on the igneous nature of the máaz formation at jezero crater and link with séítah, mars. J. Geophys. Res.: Planets 128 (7), e2022JE007440.

Viviano, C.E., Seelos, F.P., Murchie, S.L., Kahn, E.G., Seelos, K.D., Taylor, H.W., Taylor, K., Ehlmann, B.L., Wiseman, S.M., Mustard, J.F., Morgan, M.F., 2014. Revised CRISM spectral parameters and summary products based on the currently detected mineral diversity on mars. J. Geophys. Res.: Planets 119 (6), 1403–1431.

Wiens, R.C., Maurice, S., Gasnault, O., Anderson, R.B., Beyssac, O., Bonal, L., Clegg, S., DeFlores, L., Dromart, G., Fischer, W., Forni, O., Grotzinger, J.P., Johnson, J.R., Martinez-Frias, J., Mangold, N., McLennan, S.M., Montmessin, F., Rull, F., Sharma, S.K., Cousin, A., Pilleri, P., Sautter, V., Lewin, E., Cloutis, E.A., Poulet, F., Bernard, S., McConnochie, T.H., Lanza, N.L., Newsom, H.E., Ollila, A.M., Leveille, R., Le Mouélic, S., Lasue, J., Melikechi, N., Meslin, P.-Y., Grasset, O., Angel, S.M., Fouchet, T., Beck, P., Bousquet, B., Fabre, C., Pinet, P., Benzerara, K., Montagnac, G., Arana, G., Castro, K., Laserna, J., Madariaga, J.M., Manrique, J.A., Lopez, G., Lorenz, R., Mimoun, D., Acosta-Maeda, T., Alvarez, C., Dehouck, E., Delory, G., Doressoundiram, A., Francis, R., Frydenvang, J., Gabriel, T., Jacob, X., Madsen, M.B., Moros, J., Murdoch, N., Newell, R.T., Porter, J., Quantin-Nataf, C., Rapin, W., Schröder, S., Sobron, P., Toplis, M.J., Brown, A.J., Veneranda, M., Chide, B., Legett, C., Royer, C., Stott, A., Vogt, D., Robinson, S.H., Delapp, D., Clavé, E., Connel, S., Essunfeld, A., Gallegos, Z.E., Garcia-Florentino, C., Gibbons, E., Huidobro, J., Kelly, E., Kalucha, H., Ruiz, P., Torre-Fdez, I., Shkolyar, S., 2021. SuperCam on the perseverance rover for exploration of jezero crater: remote LIBS, VISIR, Raman, and time-resolved luminescence spectroscopies plus micro-imaging and acoustics. LPI Contrib. 52 (2548), 2.

Wiens, R.C., Udry, A., Beyssac, O., Quantin-Nataf, C., Mangold, N., Cousin, A., Mandon, L., Bosak, T., Forni, O., McLennan, S.M., Sautter, V., Brown, A., Benzerara, K., Johnson, J.R., Mayhew, L., Maurice, S., Anderson, R.B., Clegg, S.M., Crumpler, L., Gabriel, T.S.J., Gasda, P., Hall, J., Horgan, B.H.N., Kah, L., Legett, C., Madariaga, J.M., Meslin, P.-Y., Ollila, A.M., Poulet, F., Royer, C., Sharma, S.K., Siljeström, S., Simon, J.I., Acosta-Maeda, T.E., Alvarez-Llamas, C., Angel, S.M., Arana, G., Beck, P., Bernard, S., Bertrand, T., Bousquet, B., Castro, K., Chide, B., Clavé, E., Cloutis, E., Connell, S., Dehouck, E., Dromart, G., Fischer, W., Fouchet, T., Francis, R., Frydenvang, J., Gasnault, O., Gibbons, E., Gupta, S., Hausrath, E.M., Jacob, X., Kalucha, H., Kelly, E., Knutsen, E., Lanza, N., Laserna, J., Lasue, J., Le Mouélic, S., Leveille, R., Lopez Reyes, G., Lorenz, R., Manrique, J.A., Martinez-Frias, J., McConnochie, T., Melikechi, N., Mimoun, D., Montmessin, F., Moros, J., Murdoch, N., Pilleri, P., Pilorget, C., Pinet, P., Rapin, W., Rull, F., Schröder, S., Shuster, D.L., Smith, R.J., Stott, A.E., Tarnas, J., Turenne, N., Veneranda, M., Vogt, D.S., Weiss, B.P., Willis, P., Stack, K.M., Williford, K.H., Farley, K.A., THE SUPERCAM TEAM, 2022. Compositionally and density stratified igneous terrain in jezero crater, mars. Sci. Adv. 8 (34), eabo3399.

Zastrow, A.M., Glotch, T.D., 2021. Distinct carbonate lithologies in jezero crater, mars. Geophys. Res. Lett. 48 (9), e2020GL092365.